Cryogenics at the BENSC Millikelvin Laboratory

Scientific highlights
Structural Research 2005

Photo: Bernhard Schurian

X-rays help find out how parts of historic organs were made

A. Manescu[1], A. Giuliani[1], F. Fiori[1], B. Baretzky[2]
■ 1 Università Politecnica delle Marche, Dipartimento SASC, Ancona, Italy ■ 2 Max-Planck-Institut für Metallforschung, Stuttgart, Germany

Fig. 1: Organ in the Holy Ghost (Dominican Church) in Vilnius (Lithuania) built by Adam Gottlob Casparini (1715–1788) and completed in 1776. Brass tongues from similar organs were investigated in the experiments described in the present article.

Introduction

The organ, one of the most sophisticated musical instruments, is an important symbol of European culture. Nowadays, one of the main problems organ builders have to confront is the difficulty in obtaining the warm and beautiful sound of historic organs by using modern materials and technologies. Achieving true Baroque sound requires overcoming significant materials science challenges, as it is known that the alloy composition and properties of the pipes strongly influence the organ sound [1]. An organ contains flue and reed pipes made of lead-tin alloys. There are no moving parts within a flue pipe. Reed pipes, however, contain an additional vibrating part, the copper-based alloy tongue that crucially influences its sound (see Fig. 3). A reed pipe produces a sound when wind entering the bottom of the pipe causes the small brass tongue to vibrate against the shallot. The sound produced this way is amplified then by the resonator.

Fig. 2: The brass tongues from a baroque organ during the investigation at the EDDI beamline operated by the Hahn-Meitner-Institut at the synchrotron radiation source BESSY

We focused our research on determining the residual stresses – inner stresses present in the metallic material – of these brass tongues. From the literature [2] we found out the main processes the tongues were submitted to: hammering, cutting into a neat shape, annealing, filing to achieve a neat thickness and inducing of the needed curvature at the end of the manufacturing cycle.

Hammering induces compressive residual stresses in the surface layers of the tongue. Annealing relaxes such stresses. In order to bring the tongue to the optimal thickness it is filed. It is important that the tongue is filed equally across its whole width so it is not distorted when vibrating [3]. Mechanical surface processing like grinding or filing are well known to have a deep impact on materials inducing further residual stresses. In order to be able to vibrate, the tongue must have a curvature at its free end, the other end being fixed by the wedge in the block. This curvature induces opposite residual stresses, tensile in the concave side and compressive in the other side of the tongue. However, the curvature induced stresses should be low due to the low level of the curvature.

In conclusion, the stress profiles in the brass tongues are the result of stress overlapping due to different manufacturing processes. As very few information from Baroque organ builders is available, the information obtained from the residual stress analysis is important because it gives modern organ builders a confirmation regarding the processes the tongues were submitted to and it helps them in their work of trying to reproduce the warm and beautiful sound of old organs. For determining the residual stresses at different depths in the organ tongues we chose to perform an energy dispersive diffraction experiment using white beam synchrotron radiation, i.e. synchrotron radiation containing a wide range of wave lengths. As residual stresses lead to distortions in the crystal structures of the crystallites making up the material, they can be detected using diffractive methods. Using a white beam, we not only recorded simultaneously a multitude of reflections in a single energy spectrum, but we also obtained additional depth information because the reflections differ in their energy, which is directly related to the material absorption.

The Experiments

We received historic tongues from the following organs:

- Henk van Eeken, Netherlands, XVIII century
- Rimantas Gucas, Lithuania, XVIII century, Organbuilder: Jansen
- Mats Arvidsson, Överselö Church (Sweden), 1754, Johan Gren & Peter Stråhle
- Henk van Eeken, Magnuskerk Anloo (Netherlands), 1719, Organbuilder: Johannes Radeker and Rudolf Garrels
- Rimantas Gucas, Lithuania, 1780, Organbuilder: Miknevičius

The experiments were performed at the Berlin synchrotron source BESSY on the EDDI-beamline operated by the Hahn-Meitner-Institut. We used white radiation in an energy range from 10 to about 100 keV provided by a 7T multipole wiggler. The average dimensions of the samples were: $120\text{mm} \times 15\text{mm} \times 0.7\text{mm}$. We analysed each organ tongue in three areas (see Fig. 4).

Results

We observed the presence of compressive stresses in all the analysed samples, close to the surface of the tongues, due to the process of hammering. These stresses vary from sample to sample, depending on the force applied during hammering and depending on possible annealing treatments, between sequential hammering cycles, that partially relax such compressive stresses. We can consider the orthogonal stress as being the stress induced by hammering-annealing processes. In all samples, the orthogonal stresses remain constant in the different analysed points on the front side and also in the point on the back side of the tongues. The next result is that from a qualitative point of view and close to the sample surface, after the filing treatments, all the samples exhibit, in the direction parallel to the process a relaxation of the compressive stress induced by hammering. Also, a clear difference in some tongues can be observed between the values of the residual stresses in the filing direction in the fixed, middle and vibrating points. The tongues were more filed in the middle and vibrating part than in the fixed part. In four of the five analysed tongues, we observed less compressive stresses in the parallel direction in respect with the orthogonal direction for both sides of the tongues, which means that the filing was performed both on the front and on the back side of the tongues.

In conclusion, the energy dispersive diffraction experiment performed on historic brass tongues allowed us to identify the main manufacturing processes the tongues were submitted to, giving this way precious information to the organ builders in their work of reproducing the beautiful sound of Baroque organs.

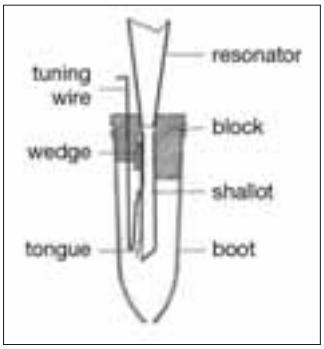

Fig. 3: Scheme of a reed pipe

Acknowledgements

The authors would like to thank Dr. Christoph Genzel and his team at the outstation of the Hahn-Meitner-Institut at BESSY for their theoretical and experimental support, Prof. F. Rustichelli for consultation on tongue processing effects on residual stresses. They are further indebted to the Hahn-Meitner-Institut and BESSY for beamtime allocation. This research project has been supported by the European Commission under the 6th Framework Programme through the Key Action: Strengthening the European Research Area, Research Infrastructures. Contract n°: RII3-CT-2003-505925 (NMI3). Finally the authors wish to express their thanks to the TRUESOUND European Project (CT.FP6-2002-SME-1 005876) partners, for the availability of the organ brass tongues and their precious consultation.

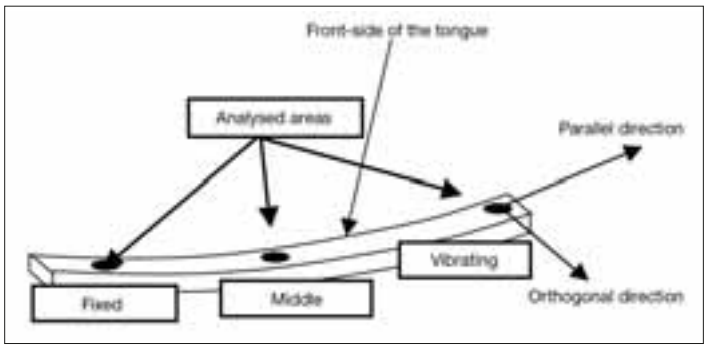

Fig. 4: Measurement points and directions in the investigation of organ tongues by x-ray diffraction

[1] M. Kob, Acta Acustica 86 642–648 (2000); W. Kluge, Acta Organologica 15 181–212 (1981)

[2] R. Gug, *Historic and experimental studies on brass used for reed tongues*, FOMRHI-Quarterly, 41, Oxford (1998)

[3] Geoffrey Crabb, *Concertina Reed Production – The Crabb Method*, http://www.concertina.net/gc_make_reeds.html, 2003

Corresponding author:
A. Manescu
a.manescu@alisf1.univpm.it

Magnetic field-induced antiferromagnetism in a cuprate high-temperature superconductor

B. Lake[1,2], K. Lefmann[3], N. B. Christensen[3], G. Aeppli[4], D. F. McMorrow[3,4], H. M. Ronnow[5], P. Vorderwisch[1], P. Smeibidl[1], N. Mangkorntong[6], T. Sasagawa[6], M. Nohara[6], H. Takagi[7]

■ 1 HMI ■ 2 Ames Laboratory and Department of Physics and Astronomy, Iowa State University, Ames, USA ■ 3 Materials Research Department, Risø National Laboratory, Roskilde, Denmark ■ 4 London Centre for Nanotechnology and Department of Physics and Astronomy, University College London, London, UK ■ 5 Laboratory for Neutron Scattering, Paul-Scherrer-Institut & ETH-Zurich, Switzerland ■ 6 Department of Advanced Materials Science, University of Tokyo and CREST-JST, Kasiwa, Japan ■ 7 RIKEN (The Institute of Physical and Chemical Research), Wako, Japan

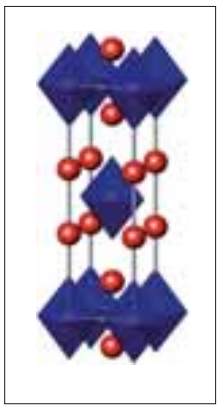

Fig. 1: Structure of a $La_{2-x}Sr_xCuO_4$ (LSCO) crystal. The red balls stand for the lanthanum or strontium atoms. The oxygen atoms are located at the vertices of the blue octahedra, the copper atoms at their centres. Superconductivity occurs in the horizontal planes defined by the copper and oxygen atoms.

High temperature superconductors have been an active area of research for the past 20 years. The materials consist of nearly square CuO_2 lattices alternating with LaO charge reservoir layers (Fig. 1). Replacing Lanthanum (La) with Strontium (Sr) – hole-doping – gives rise to superconductivity for certain concentrations of Sr. They are described as strongly correlated electron systems where exotic behaviour arises from competition on a quantum mechanical level involving collective electronic states such as antiferromagnetism, charge stripe order, non-fermi liquid behaviour as well as superconductivity. The mechanism for the superconducting process is not yet understood and is an active research field. In an applied magnetic field high temperature (high-T_c) superconductors behave like type-II superconductors: magnetic flux is able to penetrate the system via the formation of vortices, which are normal state metallic cylinders each carrying one flux quantum. The vortices form a lattice of resistive material embedded in the non-resistive superconductor. The vortex density increases with increasing field, and when the upper critical field H_{c2} is reached, superconductivity is destroyed altogether.

In the high-T_cs the superconducting coherence length is anisotropic and small, in fact it is less than the separation of the copper oxide planes. This means that three-dimensional superconductivity is only achieved via Josephson coupling between the planes. The superconducting coherence length is also a measure of the vortex size and the vorticies are best regarded as two-dimensional disks or 'pancakes'. Couplings regulating the stacking of the pancakes are therefore important for the establishment of phase coherent superconductivity in applied magnetic fields.

Here we discuss the effects of applied magnetic field on the high temperature, cuprate superconductor $La_{2-x}Sr_xCuO_4$ (LSCO) with $x = 0.10$ and a superconducting transition temperature of $T_c = 29\,K$. Previous measurements on LSCO indicate weak, long-period magnetic order in zero-field derived from defects which differ from sample to sample, and stronger field-induced order with all of the hallmarks of an intrinsic effect [1], including sample-independence and a sharp onset temperature indistinguishable from T_c. In all previous experiments the field was vertical and perpendicular to the CuO_2 planes. This precluded an examination of the important inter-planar magnetic correlations. In these current measurements the field is now horizontal, allowing the field to be applied along the c direction and at the same time giving access to the out-of-plane magnetic correlations. What makes this experiment much more difficult than previous measurements is the restricted access of the neutron beam to the sample in the more complex magnet and the imperfect match between the signal shape (in reciprocal space) and the instrument resolution function.

The antiferromagnetic order was measured by neutron diffraction using the V2/FLEX triple axis spectrometer and the HM1 horizontal field magnet (Fig. 2). The details of the experiment are discussed in detail in the original publication [1]. In this report, we concentrate on the interpretation of the results.

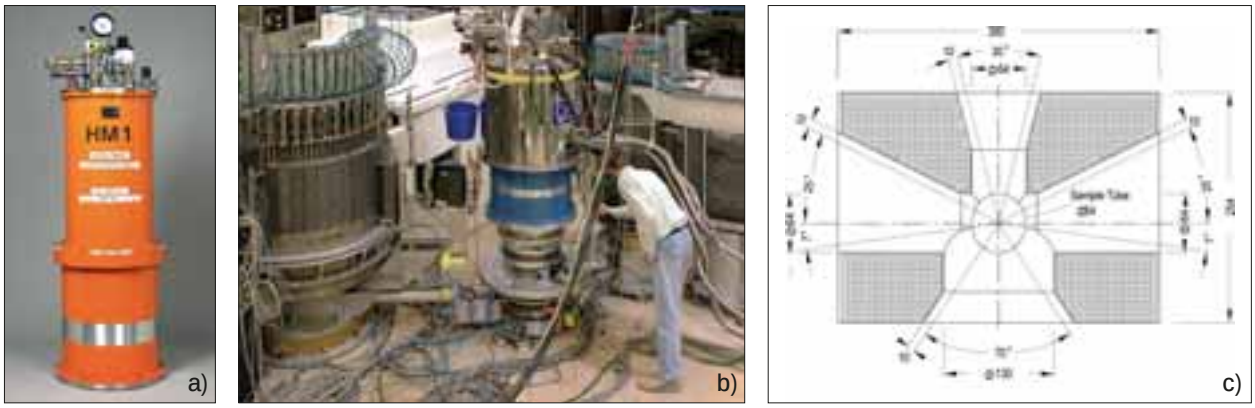

Fig. 2: a) The horizontal field magnet HM1 b) The Triple-Axis-Spectrometer V2/FLEX with a different cryomagnet mounted than the one used in the experiment c) Cross-section of the horizontal-field magnet (HM1). The magnet has four windows through which neutrons can pass, separated by four blind spots (hatched regions) which are opaque to neutrons. The LSCO crystal lies at the centre of the magnet.

Fig. 3a and 3b show a potential model of the zero-field order, the black dots represent the Cu^{2+} ions and the red arrows attached to them represent both the size and relative ordering direction of their spin moments. We envisage that there are magnetic regions within the crystal possibly nucleated by defects. These magnetic patches have large spatial extent within the CuO_2 planes. They however have only small spatial extent perpendicular to the CuO_2 planes giving rise to weak modulations in that direction. When a magnetic field is applied to LSCO, vortices are formed which thread through the superconductor parallel to the field. For a field applied parallel to c the vortices would be able to link the pre-existing antiferromagnetic regions along this direction providing a mechanism by which the magnetic correlations between the CuO_2 layers are enhanced (Fig. 3b). The increased magnetic correlation length in the out-of-plane direction would be observed as an enhancement of the magnetic signal at the reciprocal lattice points as found experimentally.

These results are interesting for a number of reasons, firstly they imply that the field-induced magnetism is an intrinsic property of this material, secondly they shows that a magnetic field can be used to tune the degree of interlayer coupling while at the same time varying the onset temperature for phase coherent superconductivity. Thirdly our results link the field-induced magnetism directly to the formation of vortices revealing the close interplay between magnetism and superconductivity in the high-T_cs.

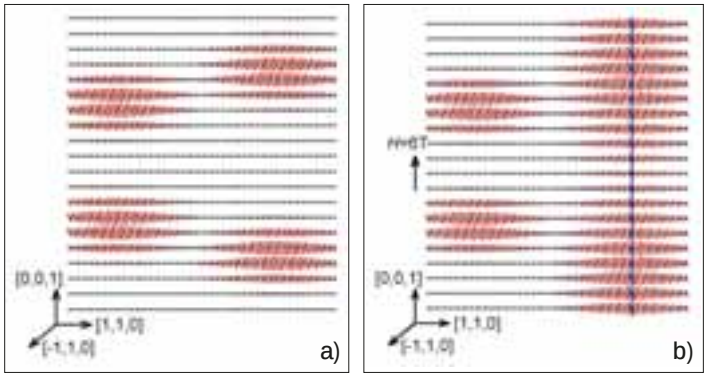

Fig. 3: Interpretation of the neutron scattering data. In zero field, a), defects nucleate magnetically ordered regions. The defects are located on the LaO_2 planes and give rise to ordering in the neighbouring CuO_2 planes; in the diagram, only the magnetic Cu^{2+} ions are shown, these are represented by the black dots while the size and direction of their ordered moments are represented by the red arrows. The magnetic regions are limited to a few CuO_2 planes, but have large spatial extent within the planes (reduced here for visualization) and they are characterised by an inversion in the magnetic ordering at the bond-centred defect site. When a magnetic field is applied along the c-axis, vortices thread through the material parallel to the field. If a vortex (blue line) passes through a magnetically ordered region it increases the number of planes over which ordering extends as shown in b).

[1] B. Lake, et al. Nature Materials 4, 658–662 (2005)
[2] B. Lake, et al. Nature 415, 299–302 (2002)
[3] T. Suzuki, et al. Phys. Rev. B 57, R3229–R3232 (1998)
[4] Xu, G.Y., et al. Science 289, 419–422 (2000)

Corresponding author:
B. Lake
bella.lake@hmi.de

Neutron diffraction studies of R_2Fe_{17} (R=Y, Lu) intermetallics under pressure

J. Kamarád[1], O. Prokhnenko[1,2], K. Prokeš[2], Z. Arnold[1]
■ 1 Institute of Physics AS CR, Prague, Czech Republic ■ 2 HMI, SF2

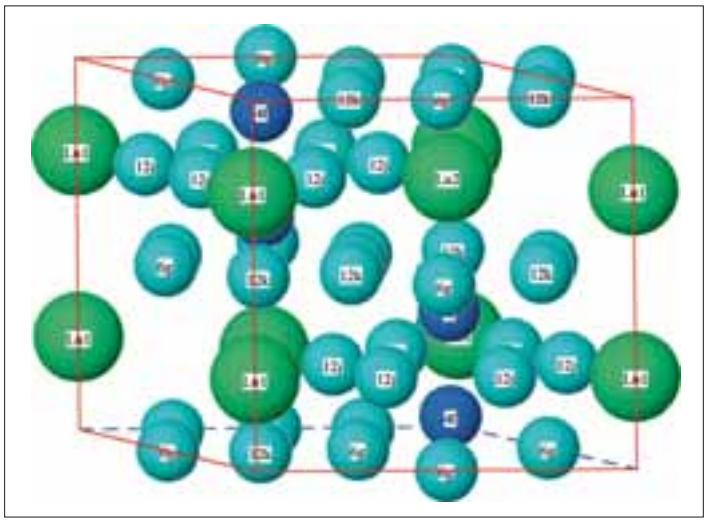

Fig. 1: Schematic representation of the layered crystal structure of Lu_2Fe_{17}. One hexagonal unit cell contains four lutetium (Lu) atoms in two inequivalent positions and thirty-four Fe atoms in four different crystallographic positions that are indicated by the so called Wyckoff symbol.

There are two main conditions for the occurrence of magnetic ordering: the existence of individual magnetic moments and the strength of an exchange interaction between the moments. Both factors depend mainly on the type, distances and geometry of the arrangement of atoms involved and can be influenced by temperature (thermal movement tries to destroy the geometrical arrangement of the moments, magnetic order exists only below a critical temperature), pressure (pressure compresses the atoms closer to each other destabilizing the individual moments) and magnetic fields (moments try to minimize their energy with respect to the field by rotating to an energetically more favourable orientation – this may change the type of order).

There are many types of magnetic ordering. The two basic types are

1. ferromagnetism: below the so called Curie temperature T_C, all moments point in the same direction leading to a non-zero magnetization
2. antiferromagnetism, in which below the Néel temperature T_N, for every magnetic moment pointing into one direction, there is another moment with exactly the opposite direction. This arrangement leads to zero net magnetization.

From the point of view of the direction of moments, one can distinguish between collinear magnetic structures, where all the moments point along a single direction and non-collinear, in which more directions exist.

In this contribution, one particular type of magnetic order will be discussed – helimagnetic order, in which competing exchange interactions exist. As a result, the moments are arranged ferromagnetically within the planes. The direction, however, changes by a certain angle as one moves to the subsequent plane due to antiferromagnetic interaction between the planes. So, the individual planes in helimagnetic structures are ferromagnetic, but the sample as a whole exhibits zero magnetization.

Neutron diffraction plays a crucial role in the identification of magnetic structures because the neutron's magnetic moment can interact with periodically arranged magnetic moments resulting in interference phenomena that carry useful information regarding the coupling, direction and size of magnetic moments. As neutrons only weakly interact with most elements, one can use rather complicated sample environments – required to "prepare" suitable conditions for the existence of a particular magnetic phase – in the diffraction experiments.

Recent results have again drawn attention to non-collinear magnetism in iron and its alloys. Both, theoretical and experimental studies of these structures have been intensified and great progress has been reached in a description of the spin dynamics in systems where magnetism is caused by electrons that are almost free to move (the case of Fe). Recent studies of volume-change effects in the R_2Fe_{17} compounds under magnetic field with non-magnetic R-atoms (Y, Lu) have brought indispensable information [1]: Magnetization measurements showed that the ferromagnetic ordering in Y_2Fe_{17} is drastically modified under high pressure. The results indicated the presence of a pressure-induced non-collinear magnetic structure. This fact became subject of a controversy in the last decade because theoretical calculations did not indicate the instability of the ferromagnetic phase in this compound [2].

In contrast to those in Y_2Fe_{17}, the Fe-moments in Lu_2Fe_{17} order helimagnetically below the Néel temperature $T_N = 275\,K$ due to a competition of the ferromagnetic and the antiferromagnetic exchange interactions between the Fe-ions on different crystallographic sites [3]. With decreasing temperature and simultaneously increasing volume, the ferromagnetic exchange interactions dominate and helimagnetism transforms towards the ferromagnetic ground state below $\Theta_T = 140\,K$ with moments still confined within basal planes. At temperatures between T_N and Θ_T, the Fe-moments remain collinear within the basal planes, but their direction changes from plane to plane on moving along the *c*-axis. The ferromagnetic ground state of Lu_2Fe_{17} can be also totally suppressed by a mediate hydrostatic pressure.

Despite technical complexity and resulting experimental limitations, we have decided to verify the changes of the magnetic structures as a function of pressure and magnetic field on a microscopic scale. We have performed several neutron diffraction experiments on small single crystals under pressure produced by a small clamped-type CuBe pressure cell that fits into several cryomagnets available at HMI. The single crystals of Y_2Fe_{17} and Lu_2Fe_{17} were fixed inside the pressure cell and placed in a vertical superconducting magnet with the *a*-axis being parallel to the magnetic field of up to 6.5 T. A mixture of mineral oils was used as a hydrostatic pressure-transmitting medium up to pressure 1.1 GPa in the cell. The details of the experimental results can be found in the original publication [4]. Here, we discuss the conculsions concerning the observed magnetic structures.

Measurements performed at the pressure 0.8 GPa revealed a helimagnetic structure in Y_2Fe_{17} in a narrow temperature range between 235 K and 255 K. In the temperature range 230 K down to 2 K under pressure of 0.8 GPa the gradual development of the ferromagnetic component can be observed. At a pressure of 1.05 GPa, a magnetic structure was found even at 2 K. However, the scans at temperatures from 2 K up to 270 K showed that the magnetic structure disappears in an intermediate temperature range between 115 K and 150 K. It is for the first time that this kind of discontinuity has been observed in the temperature behaviour. The pressure induced magnetic phase at higher temperature differs most probably from the one at low temperature. It follows from the experiments that the ferromagnetic arrangement of Fe-moments in Y_2Fe_{17} transforms into the incommensurate helimagnetic structure with increasing pressure, i.e. with decreasing volume. At 5 K and 1.05 GPa, the angle between Fe-moments in the adjacent basal planes amounts to 19.35°.

Fig. 2: CuBe clamped cell used in the pressure experiments. Below the main body of the cell from the left to the right: the fixing screw with the manganin pressure sensor and electrical leads, piston and the opposite fixing screw.

Neutron diffraction measurements on the Lu_2Fe_{17} single crystal confirmed the existence of three magnetic phases in Lu_2Fe_{17} already at ambient pressure. At the temperature $\Theta_T = 140\,K$, a transition from the ferromagnetic ground state into the incommensurate helimagnetic structure occurs. An application of magnetic field along the *a*-axis of Lu_2Fe_{17} at 200 K results in the transition from the helimagnetic to the ferromagnetic phase. All these features show different character of the helimagnetic-ferromagnetic transitions induced by the temperature and/or forced by the magnetic field at ambient pressure. The detailed mechanism of the field induced transformation (e. g. through a distorted elliptical spiral) has to be solved unambigiously by further investigation.

Acknowledgments

The financial support of the projects 202/04/P014 GACR and AV0Z10100521 is acknowledged. This research project has been also supported by the European Commission under the 6th Framework Program through the Key Action: Strengthening the European Research Area, Research Infrastructures. Contract n°: RII3-CT-2003-505925 (NMI3)

[1] Z. Arnold, J. Kamarád, P. A. Algarabel, B. Garcia-Landa, M. R. Ibarra, IEEE Trans. Mag. **30**, 619 (1994)
[2] R.F. Sabiryanov, S. S. Jaswal, Phys. Rev. B **57**, 7767 (1998)
[3] D. Givord, R. Lemaire, IEEE Trans. Magn. MAG-10, 109 (1974)
[4] O. Prokhnenko, J. Kamarád, K. Prokeš, Z. Arnold, A. V. Andreev, Phys. Rev. Lett. **94**, 107201 (2005)

Corresponding author:
K. Prokeš
prokes@hmi.de

Use of arsenic isotopes for molecular imaging and endoradiotherapy

M. Jahn, M. Jennewein, M. Piel, F. Rösch
■ Intitute of Nuclear Chemistry, Johannes Gutenberg-University, Mainz, Germany

Positron emission tomography (PET) is a non-invasive diagnostic imaging technique for measuring the metabolic activity of cells in the human body. It is particularly useful clinically in patients with certain diseases affecting the brain, heart and in patients with certain types of cancer. PET is unique because it produces images of the body's basic biochemistry and functions. Chemical compounds are labeled with radioactive atoms that decay by emitting positrons. The positron combines with an electron in the medium and is annihilated into two 511 keV photons that are emitted in coincidence at 180°. This radiation is detected outside the body, and it is possible to localize and quantify the measured activity in vivo. The standard positron emitters ^{11}C ($T_{1/2}$ = 20 min) and ^{18}F ($T_{1/2}$ = 109 min) allow only the observation of relatively fast biological processes. In contrast the element arsenic provides a range of radioactive isotopes with potential interest in radiopharmaceutical chemistry and PET. In particular, the long half-lives of ^{72}As ($T_{1/2}$ = 26 h, 88 % β^+) and ^{74}As ($T_{1/2}$ = 17.8 d, 29% β^+) allow the investigation of slow physiological or metabolic processes, like the enrichment and distribution of antibodies in tumor tissue or cell trafficking. ^{77}As ($T_{1/2}$ = 38.8 h, 100% β^-) is used for the development of new labeling strategies with arsenic because it is easily accessible at nuclear reactors. It also might be used in tumor-targeting radiotherapeutics because of its low γ-dose rate and its moderate average β^--range (1.2 mm) in tissue. It was thus the aim of this project, to investigate (i) the production route of high batch activities of ^{77}As, (ii) its effective chemical separation and (iii) the use of ^{77}As to study radiopharmaceutical synthesis strategies with radioarsenic.

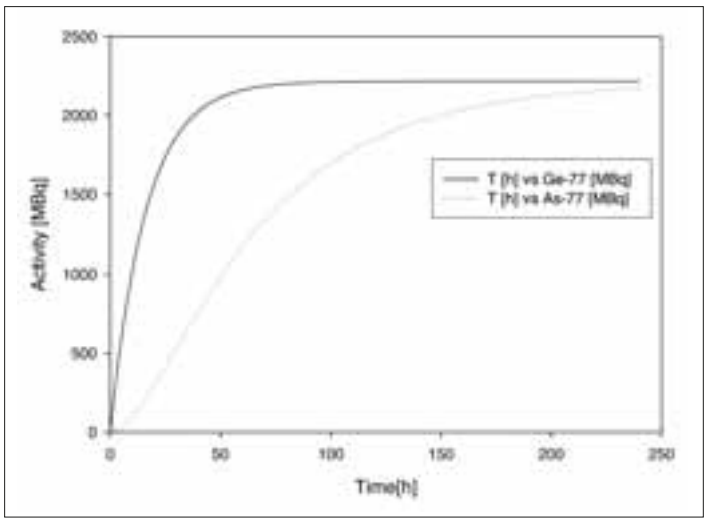

Fig. 1: Calculated kinetics of the activation of 230 mg $^{nat}GeO_2$ at BER II

Production of isotopes

All arsenic isotopes can be produced by irradiating GeO_2-Targets. ^{77}As is the most important radionuclide for the development of new arsenic radiopharmaceuticals because its production is very cheap compared to the cyclotron produced positron emitters ^{72}As and ^{74}As. These are only used when the labeling chemistry of a radiopharmaceutical has been optimized with ^{77}As. ^{77}As is produced via $^{76}Ge(n,\gamma)^{77}Ge \rightarrow \beta^-(T_{1/2} = 11.3\,h) \rightarrow {}^{77}As$ at the TRIGA reactor of the Institute of Nuclear Chemistry of the University of Mainz ($\varphi = 4.0 \times 10^{12}$ n/cm²s). All irradiations were performed using 100 mg of $^{nat}GeO_2$. Due to the low neutron capture cross section of ^{76}Ge (σ = 0.15 barn) and its low natural abundance (7.44 %), 6 h of irradiation yields about 2 MBq of ^{77}As 12 h after reactor shut down. This is enough for chemical experiments while for ERT much higher activities of about 4 GBq are needed. Thus $^{nat}GeO_2$ targets were irradiated for 96 h at the reactor BER II of the Hahn-Meitner-Institut to yield about 1.5 GBq of ^{77}As (calculated). Due to logistic problems the maximum activity isolated from the target in Mainz was about 200 MBq, so some logistics need to be optimized. For future applications the use of highly enriched $^{76}GeO_2$ targets is aimed. This would increase the maximum achievable ^{77}As activity by a factor up to 13 and simultaneously decrease the formation of byproducts like ^{71}Ge and ^{75}Ge significantly. At high flux reactors the production of enough ^{77}As for ERT is possible.

The positron emitting arsenic isotopes ^{74}As and ^{72}As are produced at cyclotrons. Indirectly, ^{72}As can be also produced as a daughter radionuclide of the relatively long-lived ^{72}Se ($T_{1/2}$ = 8.5 d). This $^{72}Se/^{72}As$ radionuclide generator [1, 2] has the advantage of avoiding cyclotron in house production of ^{72}As.

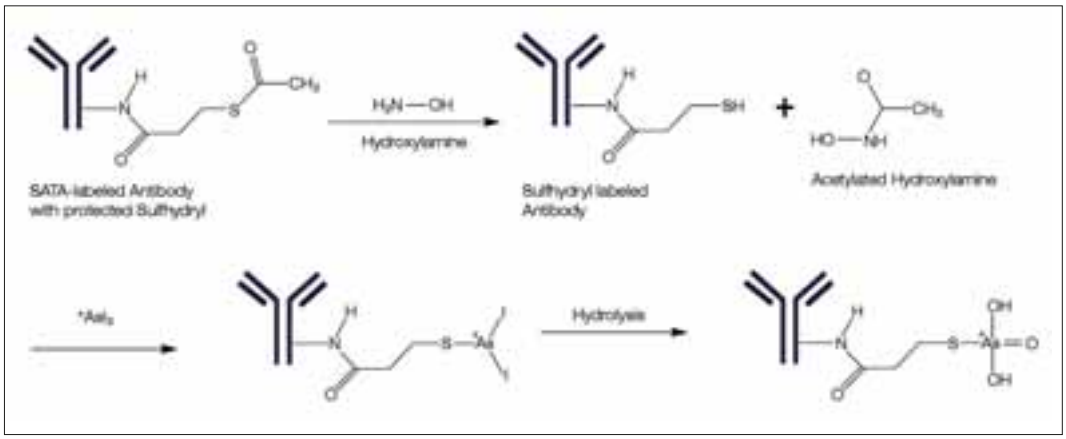

Fig. 2: Reaction scheme for labeling of SATA-modified antibodies with radioactive arsenic isotopes

Separation of arsenic from the target

Irradiated germanium oxide targets were dissolved in 5 ml HF at room temperature for 1 h whereby GeF_6^{2-} is formed [3]. Potassium iodide was added for the quantitative formation of $[^{77}As]AsI_3$. The mixture was transferred to an ENV-solid phase extraction cartridge and $[^{77}As]AsI_3$ was fixed to the solid phase, while macroscopic GeF_6^{2-} was eluted quantitatively with the mobile phase. The elution of the $[^{77}As]AsI_3$ was performed with 500–1000 µl of various organic solvents and directly used as labeling synthon.

Radiolabelling of antibodies

As a proof-of-principle study for the application of arsenic labeled compounds in biological systems, the high affinity of arsenic to sulfur was utilized to conjugate arsenic to HS-protein structure elements. SATA (N-Succinimidyl-S-acetylthioacetate) was applied [4] to increase the number of free sulfhydryls in the protein (Fig. 2). Deprotection of the sulfhydryl groups with hydroxylamine was performed directly before the labeling. For subsequent radioarsenic labelling of the proteins, a $[^{77}As]AsI_3$ containing ethanolic solution was added to the solution of the SATA modified proteins and the $[^{77}As]AsI_3$ was coupled to one SH under elimination of iodide. First biodistribution studies, autoradiography and PET of SATA-derivatised antibodies were performed (Fig. 3).

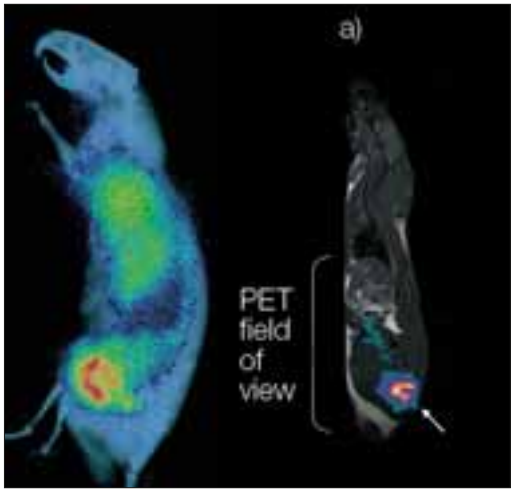

Fig. 3: Autoradiography of $[^{77}As]$SATA-ch3G4 and $[^{74}As]$SATA-ch3G4 small animal PET

[1] Jennewein, M., et al., *A no-carrier-added $^{72}Se/^{72}As$ radionuclide generator based on solid phase extraction*. Radiochimica Acta, 93 (9–10), 579–583 (2005)

[2] Jennewein, M., et al., *A no-carrier-added $^{72}Se/^{72}As$ radionuclide generator based on distillation*. Radiochimica Acta, 92, 245–249 (2004)

[3] Jennewein, M., et al., *A new method for radiochemical separation of arsenic from irradiated germanium oxide*. Appl Radiat Isot, 63 (3), 343–51 (2005)

[4] Duncan, R.J., et al., *A new reagent which may be used to introduce sulfhydryl groups into proteins, and its use in the preparation of conjugates for immunoassay*. Anal Biochem, 132 (1), 68–73 (1983)

Corresponding author:
M. Jahn
jahnma@uni-mainz.de

Where are the limits of non-exponential relaxation?

C. Pappas[1], A. Hillier[2], P. Manuel[2], R. Cywinski[3], I. A. Campbell[4], P. Bentley[1], F. Mezei[1]
■ 1 HMI, SF1 ■ 2 ISIS, Didcot, UK ■ 3 Physics and Astronomy Department, University of Leeds, UK
■ 4 Université de Montpellier 2, France

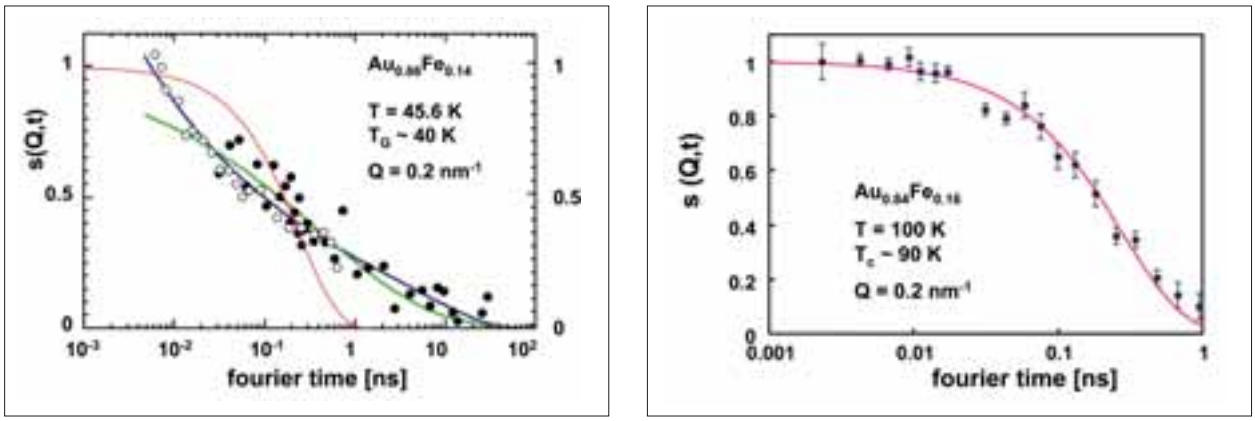

Fig. 1: NSE signal of the spin glass $Au_{0.86}Fe_{0.14}$ and the disordered ferromagnet $Au_{0.84}Fe_{0.16}$. Both spectra were collected at $Q = 0.2\,nm^{-1}$ and at 10 % above the corresponding ordering temperatures slightly above T_C. The continuous red lines are the best fit of the data to a simple exponential decay. The eminently non-exponential decay of the spin glass $Au_{0.86}Fe_{0.14}$ is best fitted by the so-called Ogielski function $t^{-x}\exp[(-t/\tau(T))^{\beta}]$ (blue line).

Non-exponential relaxation is a general phenomenon found in systems as diverse as glasses, spin glasses, heavy fermions, polymers, biological systems, financial markets, earthquakes etc. Even though these very different and complex disordered systems show strong similarities, the existence of universal relaxation functions and mechanisms is still an open question. The situation is even more complex, when disorder is too weak to completely overcome and destroy the long-ranged spatial periodical order. In systems like disordered ferro- and antiferromagnets, neutron scattering reveals a purely exponential spin relaxation in contradiction with long standing theoretical arguments first introduced by Griffiths [1], which predict anomalous effects and non-exponential relaxation [2,3]. This puzzling and enduring discrepancy between theory and experiment incites to go beyond the existing experimental results and investigate relaxation of disordered ferromagnets at different length and time scales by combining zero field muon spin relaxation (μSR), a local probe, with the mesoscopic time and length scales of Neutron Spin Echo (NSE) spectroscopy.

The solid solution $Au_{1-x}Fe_x$ is an archetype disordered ferromagnet, where the magnetic moments, carried by the Fe^{3+} ions, are randomly distributed over the non-magnetic Au fcc lattice. The oscillatory RKKY magnetic interactions lead to positive (ferromagnetic) nearest-neighbour interactions, negative (antiferromagnetic) next nearest neighbour interactions and so on. The system is a disordered ferromagnet at high Fe concentrations and becomes a spin glass at $x < x_C$, with $x_C \sim 0.155$, a concentration between the nearest neighbour and next nearest neighbour site percolation thresholds for the fcc lattice. In spite of the dilution, the strong magnetic moments of Fe^{3+} ($S = 5/2$) and their ferromagnetic correlations make this system ideal for neutron and muon spectroscopy. The samples covered the whole spectrum from the spin glass phase with $Au_{0.86}Fe_{0.14}$ ($x = 0.14$) to the disordered ferromagnetic phase with $Au_{0.84}Fe_{0.16}$, $Au_{0.82}Fe_{0.18}$ and $Au_{0.80}Fe_{0.20}$ ($x = 0.16$, 0.18 and 0.20 respectively).

At the limit of very strong disorder, in the spin glass phase for $x = 0.14$, both NSE and μSR reveal a strongly non-exponential relaxation and there is excellent agreement between the two techniques, which unambiguously proves the homogeneous character of the spin glass relaxation [4]. The agreement between μSR and NSE in the spin glass phase is in contrast with the disagreement between the two techniques in the

disordered ferromagnetic phase. A slight increase of 2 % in the Fe concentration leads to an abrupt change of the relaxation seen by neutrons as illustrated by Fig. 1. At $x = 0.14$, the spin glass intermediate correlation function is strongly non-exponential (Fig. 1a) whereas at $x = 0.16$ the relaxation of the disordered ferromagnet is purely exponential (Fig. 1b). Both spectra were measured with NSE slightly above (10 %) the corresponding ordering temperatures T_G and T_C.

The increase of the Fe concentration, however, has no dramatic effect on the μSR spectra, which remain non-exponential even well above the disordered ferromagnetic phase. As shown on Fig. 2 the μSR spectra are best fitted by the stretched exponential form $\exp[-(-t/\tau)^{\beta}]$ even for the ferromagnetic sample. Furthermore, as seen in Fig. 3, the deviations from the simple exponential decay quantified by the parameter β are basically the same at high temperatures for both the spin glass ($x = 0.14$) and the disordered ferromagnet ($x = 0.16$). In the view of the NSE results, this is a surprising finding, which for the first time unambiguously confirms Griffiths' theoretical predictions.

The puzzling discrepancy between NSE and μSR is obviously at the origin of the failure of all attempts to identify the Griffiths phase in disordered magnets with neutron scattering and macroscopic magnetization measurements up to now. In the case of disordered ferromagnets, the ferromagnetic critical phenomena and seen on NSE and magnetisation completely mask all other contributions even though the infinite ferromagnetic cluster close to the percolation threshold is extremely ramified and involves only a fraction of the magnetic moments. Muons on the other hand, average with the same probability over the local magnetic fields and see the integral of the susceptibility over the whole Brillouin zone [5]. Therefore muons are also sensitive to the relaxation of the magnetic moments besides the ferromagnetic backbone and in this case can detect the effects related to the disorder in a different way than neutrons. Furthermore, muons can follow the relaxation well above the ferromagnetic phase, at temperatures, where neutrons fail because of intensity reasons.

The comparison between muons and neutrons shows the complementarity of the two probes and is also an illustration of the complexity of disordered systems, where the combination of several techniques covering a wide phase space is obviously necessary to pin down the relevant information. The observation of the Griffiths phase by muons and of the disordered ferromagnetic

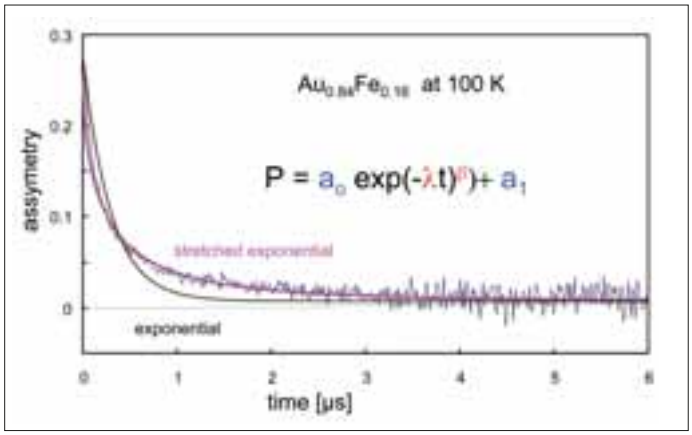

Fig. 2: Zero field μSR spectrum of $Au_{0.84}Fe_{0.16}$ at 100 K, exactly the same temperature as the NSE spectrum of Fig. 1b. The data do not follow a simple exponential and are best described by a stretched decay (see text).

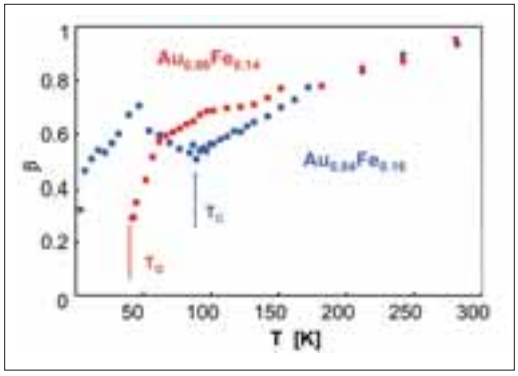

Fig. 3: Temperature dependence of the stretched exponential exponent β for the spin glass $Au_{0.86}Fe_{0.14}$ (red squares) and the disordered ferromagnet $Au_{0.84}Fe_{0.16}$ (blue squares).

transition with neutrons provides a deeper link between theory and experiment and gives a natural explanation of the marked influence of strong disorder on the ferromagnetic and antiferromagetic second order phase transitions [6].

[1] R. B. Griffiths, Phys. Rev. Lett. **23**, 17 (1969)
[2] M. Randeria, J. P. Sethna and R. G. Palmer, Phys. Rev. Lett. **54**, 1321 (1985)
[3] R. G. Lloyd, P. W. Mitchell, J. Phys. C **1**, 5013 (1989)
[4] C. Pappas, F. Mezei, G. Ehlers, P. Manuel, I. A. Campbell, Phys. Rev. B **68**, 054431 (2003)
[5] S. W. Lovesey, E. B. Karlsson, K. N. Trohidou, J. Phys.: Condens. Matter **4**, 2043 (1992)
[6] C. Pappas, M. Alba, A. Brulet, F. Mezei, J Appl. Phys. **79**, 6158 (1996)

Corresponding author:
C. Pappas
pappas@hmi.de

Time scale of nuclear fission: fast or slow?

C.-M. Herbach, D. Hilscher, U. Jahnke, V. Tishchenko
■ HMI, SF1 in collaboration with FZ Jülich, GANIL (Caen, France) and University of Rochester (USA)

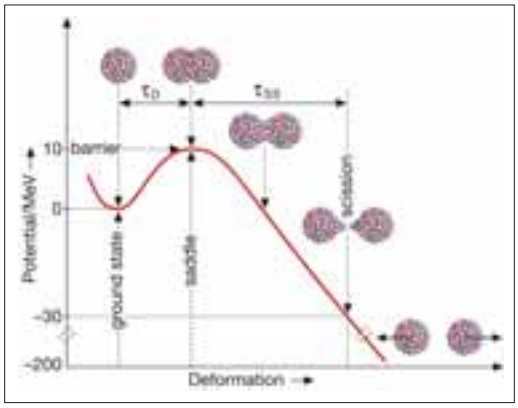

Fig. 1: Sketch of the potential energy as a function of deformation with the transient time τ_D and the saddle-to-scission time τ_{SS} indicated

Nuclear fission[1] denotes the binary splitting of a heavy nucleus into two fragments of roughly equal size. Obviously, this process implies an enormous distortion of the shape of the heavy nucleus: It has to deform axially to cigar-like shape which is further on constricted to dumbbell shape. Somewhere along this course of deformation the system reaches the saddle point in the potential energy (Fig. 1) or the fission barrier, where the short-range attractive nuclear forces become compensated by the Coulomb repulsion of the protons inside the nucleus, and from then on the pre-fragments separate under the Coulomb repulsion until the neck between them ruptures at the scission point.

Fig. 2: The NESSI detector at the COSY accelerator

It is this large-scale collective motion and its close connection to the still poorly known properties of nuclear matter such as dissipation or viscosity which makes fission so fascinating to this day: Does nuclear matter behave like a thin fluid such as water or viscous like honey or, alternatively, is the fission process fast or slow?

This problem is nearly as old as all our knowledge about fission. The importance of dissipation/viscosity for fission was recognized [1] right from the very beginning of fission research and it was argued that a purely static description of fission, i. e. considering nothing but phase space, might not be adequate.

Part of this problem was already solved some 15 years ago in favor of a large viscosity by the well known neutron clock experiments [2]. They have shown that the highly-excited compound nucleus releases most of its energy by evaporation of neutrons prior to scission, or that the total fission process is much slower than evaporation. The neutron clock experiments determine, however, the viscosity rather close to the end of the fission reaction, i. e. at low temperature and large deformation and do not allow for conclusions on a variation of the viscosity with these parameters.

The fission probability $P_f(E^*)$ as a function of excitation energy E^*, the primary objective of our investigation, instead, provides insight into dissipation or viscosity at small deformation and high excitation. This is because fission is decided upon at the saddle point and thus at small deformation and high excitation. The saddle point is, so to say, the point of no return: Any further elongation drives the system irreversibly towards scission.

Once more here, before the collective flow reaches the saddle, the nucleus is subject to evaporation. However, now at high temperature the particle emission times are much shorter than near scission. A dynamic hindrance of fission or a long transient delay τ_D for fission would thus strongly favor neutron and proton emission and thus reduce the systems fissility. Conversely, low viscosity at the saddle or a minimum transient delay τ_D tends to keep fission competitive with particle evaporation even at high excitation. The fission probability, hence, reflects the magnitude of nuclear viscosity/dissipation at high E^* and low deformation.

[1] More than six decades of extensive research in fission have elapsed since its discovery in 1938 by Hahn and Straßmann. But due to the extreme complexity of this many-particle process there is still no comprehensive dynamical model for it available – which did, however, not hamper the well known applications of fission.

Our experiments [3] were performed within the NESSI-collaboration (HMI, FZJ, GANIL, Univ. Warsaw and Univ. Rochester) aiming at the systematic investigation of GeV-proton spallation reactions for the European Spallation Source (ESS) project.

We have used the 2.5 GeV proton beam from the COSY accelerator at FZJ in order to excite 3 target nuclei, Au, Bi, and U with largely different fission barriers of 21, 12, and 5 MeV, respectively. The fission probability $P_f(E^*)$, i.e. the portion of all reactions which lead to fission, was measured up to $E^* = 1000$ MeV with our unique NESSI-detector [4] (Fig. 2) which registers virtually all emissions, neutral and charged, from the de-excitation process.

Figure 3 exhibits the experimental $P_f(E^*)$ and compares it to a simple statistical model simulation which does not account for the expected dynamic hindrance of fission. It is obvious that these calculations reproduce the characteristically different trends in $P_f(E^*)$ for Au, Bi, and U at lower E^* as well as the almost equal P_f at the highest E^* nearly quantitatively, and, most importantly, they do so *without adding any additional transient time*. Fig. 3 also shows (red dashed histogram) a calculation for p+Au where an additional delay time of $\tau_D = 2 \times 10^{-21}$ s has been introduced, which was found indispensable in a recent investigation at GSI [5]. This calculation clearly contradicts our measurement at low as well as at high E^*.

It is furthermore noteworthy that the experimental $P_f(E^*)$ for Au and U is very similar to what has been observed with antiproton reactions at LEAR/CERN [6] and thus does not depend on the particular mode of excitation.

In the same experiment we also determined the saddle-to-scission time, τ_{SS}, and as a matter of fact this was the first experiment in which both essential fission times, τ_D and τ_{SS}, were deduced simultaneously. Fig. 4 shows as an example of this investigation the energy spectra of α-particles which are emitted at $E^* = 600$ to 900 MeV either in the flight direction of the fission fragments or rather in the direction of the motion of the compound nucleus before scission. Their closer analysis shows that only about 20 % of the α-emission originates from the separated fragments, while 80 % is emitted prior to scission. The fragments are, hence, relatively cold at scission and the evaporation cascade is much faster than the fission process – in complete agreement with previous observations [2].

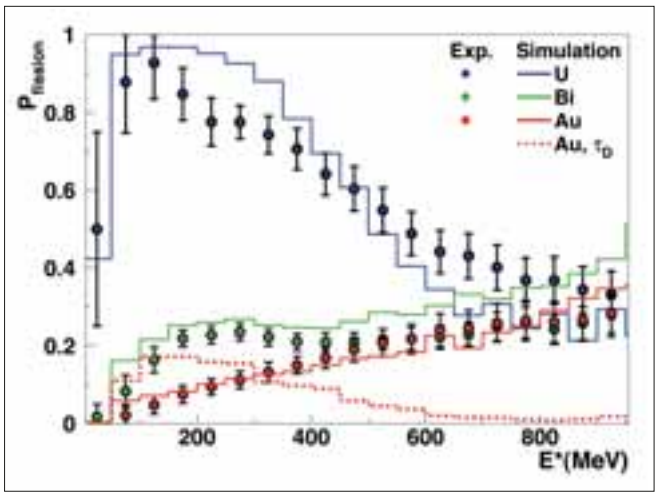

Fig. 3: Comparison of experimental and simulated fission probability as a function of E^*

In summary, we have shown that fission is decided upon on a *very fast time scale* with no dynamic hindrance and, by contrast, that the total fission process is slow compared to evaporation. Thus, nuclear dissipation or viscosity either seems to vary with temperature or with deformation.

[1] H. A. Kramers, Physica VII, no. 4, 284 (1940)
[2] D. Hilscher et al., Phys. Rev. Lett. 62, 1099 (1989)
[3] V. Tishchenko, C.-M. Herbach, D. Hilscher, U. Jahnke, J. Galin, F. Goldenbaum, A. Letourneau, W.-U. Schröder, Phys. Rev. Lett. 95, 162701 (2005)
[4] U. Jahnke et al., Nucl. Instrum. Methods A 508, 295 (2003) and C.-M. Herbach et al., ibid. A 508, 315 (2003)
[5] B. Jurado et al., Phys. Rev. Lett. 93, 0725501 (2004)
[6] U. Jahnke et al., Phys. Rev. Lett. 83, 4959 (1999)

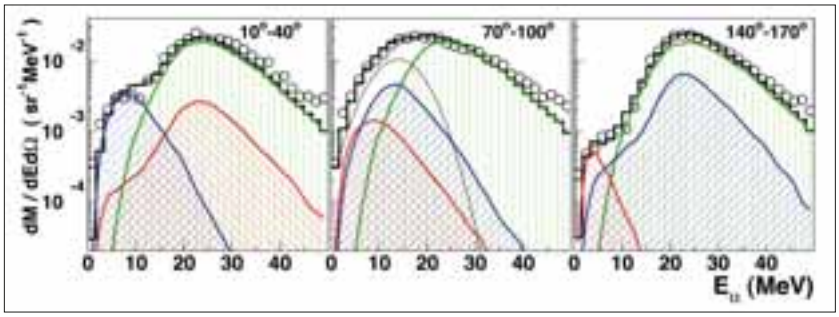

Fig. 4: Energy spectra of alpha-particles emitted in the flight direction of the light (left), the heavy (right) fission fragment or the heavy nucleus before fission (middle). The green histograms exhibit the strong emission before scission. Emission from the light and heavy fragments is shown in red and blue, respectively.

Corresponding author:
U. Jahnke
jahnke@hmi.de

Probing magnetic complexity in cobalt nanoparticles

P. Imperia[1], D. Schmitz[1], H. J. Maletta[1], J. Bansmann[2], P. Andreazza[3]
■ 1 HMI, SF2 ■ 2 Institut für Physik, Universität Rostock, Germany ■ 3 Centre de Recherche sur la Matière Divisée, France

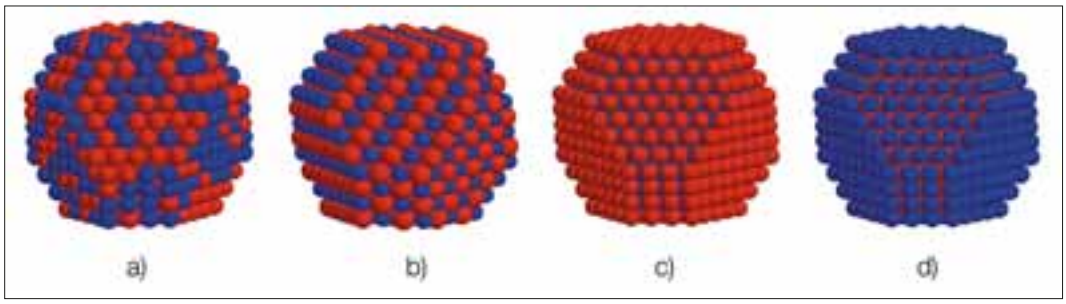

Fig. 1: Snapshots of the 807-atoms (around 2.5 nm size) platinum/cobalt Wulff polyhedral nanoparticles (blue spheres stand for Co atoms and red spheres for Pt): chemically disordered (a), ordered L10 (b), Pt surface segregated (c) and Co surface segregated model (d)

Magnetism in nanosized metallic particles with diameters in the range from 2 nm to 100 nm might hold the key to the future of magnetic memory devices. These tiny particles, composed of between a few hundred and a few tens of thousands of atoms, truly bridge the scales between the more familiar single atomic and solid state worlds. They show new physical properties different from those present in both: the isolated atom and the bulk. In fact, it is the significant proportion of atoms lying at the surface of the clusters and their interaction with the core that lies at the heart of the distinctive emergence of novel magnetic behaviour at cluster size. The orbital and spin magnetic moments (μ_l and μ_s) carried by the atoms in the cluster differ not only from the bulk material, but do so in a way that holds the promise of leading to technological applications. Electron d-bands at the surface in iron or cobalt nanoparticles narrow significantly and produce those higher orbital moments and enhanced magnetic moments that are important technologically. Understanding these small clusters and their processing thus provides fascinating scientific challenges of wide potential impact.

The ability to produce batches of nanoparticles with a high degree of uniformity in size (monodispersity) and properties is essential for their application and elucidation. Chemical synthesis provides one of the most promising routes for the industrial synthesis of the particles, and the production of cobalt and iron nanoparticles [1] has become simple and inexpensive. However, cleaning the surfactants involved in synthesis off the nanoparticles is far from trivial and oxidised surfaces readily develop [2]. Using *in situ* sample preparation techniques – portable clusters sources [3] attached to the ultra high vacuum (UHV) chambers on our beamlines – allows us to deposit monodisperse batches of pristine nanoparticles on a host of different substrates for study. The metallic clusters are produced by erosion from a hollow cathode of highly pure material. So far, particles of sizes ranging from 1 to 15 nm as well as bimetallic nanoparticles prepared by vapour deposition have been studied. It has been found that unusually well defined crystallographic structures in cobalt and cobalt/platinum core/shell nanoparticles are stabilised on specially prepared silicon substrates making them of particular interest [4], and the core/shell systems with a platinum core, ferromagnetic cobalt shell and an antiferromagnetic shell of cobalt-oxide wrapped around it, display a very high ratio of orbital to spin moment. To probe the intricate interplay of magnetism in these tiny particles requires a technique of great versatility and sensitivity. Synchrotron X-rays provide photon beams of the intensity needed for these tiny samples and X-ray magnetic dichroism (XMCD) can pick out the magnetic state in each of the constituent elements in a selective way.

In XMCD, photoabsorption spectra are recorded around the L edges of Co, Fe or Ni. Then, the magnetic orbital and spin moments can be calculated independently by integrating the difference and the sum of the spectra recorded by shining the samples with circular polarized light of opposite direction according to the sum rules [5]. Absorption spectroscopy is a surface sensitive and material selective technique, and the magnetic properties of each of the constituent atomic species can be deduced separately. However, in order to measure magnetic dichroism one has to use magnetised samples. Our ability to investigate such nano-range particles has been significantly enhanced by the commissioning (in 2005) of a new high-field chamber at the beam line UE46 PGM operated by the Hahn-Meitner-Institut which is specially designed for the application of fields up to $7\,\mathrm{T}$ at temperatures as low as $2.6\,\mathrm{K}$. Combined with the high density of photons delivered by an APPLE II type undulator at the 3rd generation synchrotron radiation source BESSY and state of the art instrumentation (including a choice between a focused beam of $16\times64\,\mu\mathrm{m}^2$ or a parallel beam of $1\times1\,\mathrm{mm}^2$), the set-up allows experiments to be performed on small atomic clusters with a low surface coverage at which the clusters are non interacting.

To gauge the impact of processing on the final magnetic properties, nanoparticles obtained with different kinds of preparation techniques have now been investigated. Chemically synthesized cobalt nanoparticles were studied in a range of post preparation surface treatments to assess the residual surfactant (oleic acid) load and cobalt oxide (CoO) surface layering. In-situ Ar^+ ion sputtering [2] effectively removes the surfactants but leaves the oxide layer. Using H^+ ions as well, however, cleaned off the oxide layer [2]. The processing also impacts significantly on the magnetic properties with Ar^+ sputtering strongly enhancing the orbital versus the spin moment which is a somewhat unexpected consequence of surface damage to the nanoparticles: Ar^+ bombardment disrupts the surface integrity and reduces crystal field quenching of orbital moments. This change in orbital moment can be measured as a function of processing time and conditions and the properties optimised. Treatment by H^+ ions alone [2], in contrast, cleans off the CoO layer and causes little surface damage leaving magnetic properties much more similar to those observed in bulk material.

Investigations of cobalt clusters in their pristine state on different substrates [3] show that the choice of the substrate provides control of the magnetic properties, as well. While cobalt clusters grown on ferromagnetic substrates show no enhanced orbital moments, clusters grown on a non-magnetic surface like gold or silicon oxide (SiO_2) have strongly enhanced values of the important orbital to spin moment ratio. A further enhancement has been observed upon exposing the samples to a small amount of oxygen. Nanoparticles with a diameter of $9\,\mathrm{nm}$ oxidised with $500\,\mathrm{L}^*$ of oxygen, show a strong increase in the ratio from $\mu_l/\mu_S = 0.08$ (clean cobalt clusters) to $\mu_l/\mu_S = 0.16$ after oxygen exposure. Simultaneously, the spin moment decreases from $\mu_S = 1.5\,\mu\mathrm{B}$ to $\mu_S = 0.7\,\mu\mathrm{B}$. Indeed, the findings on the oxidised nanoparticles point to a novel spin reorientation transition driven by the structural characteristic of the interface between the ferromagnetic and the non-magnetic substrate.

Fig. 2: The new ultra high vacuum high magnetic field reflectometer at UE46 PGM, BESSY

The results found show how the engineering of the samples leads to different magnetic properties of the nanoparticles. Further studies and more detailed analysis based on improved data sets will allow a better understanding of the complex interplay between structure, composition, size and the magnetic properties in the “nano world”.

Acknowledgements
The technical assistance of S. Rudorff as well as the continuous support and encouragement of E. Holub-Krappe, H. Rossner and A. Tennant are kindly acknowledged.

*L is the symbol of the unit langmuir. 1 L corresponds to the exposure of a surface to a gas at 10^{-6} torr for 1 second.

[1] C. B. Murray et al., IBM J. Res. & Dev. 45, 47 (2001)
[2] P. Imperia et al., Phys. Rev. B 72, 014448 (2005)
[3] J. Bansmann et al., Appl. Phys. A 82, 73 (2005)
[4] P. Andreazza et al., submitted to Nucl. Instr. and Meth. B (2005)
[5] B. T. Thole et al., Phys Rev. Lett. 68, 1943 (1992); P. Carra et al., Phys Rev. Lett. 70, 694 (1993)

Corresponding author:
P. Imperia
imperia@hmi.de

Climbing spin spirals: towards new magneto-electric materials

D. N. Argyriou
HMI, SF2

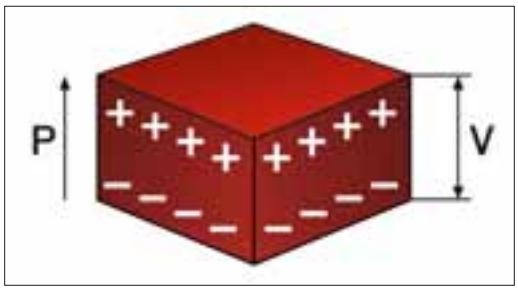

Fig. 1: In a ferroelectric material, electrical dipoles are created due to the movement of positively charged ions relative to negatively charged anions. If the dipoles point all in the same direction, the crystal is said to be polarized. The result is an electrical potential difference in a single crystal of a ferroelectric as shown above.

Ferroelectrics are one of the triumphs of modern materials science as they form the basis of a number of valuable instruments. From ultrasound machines that make images of the internal organs in our bodies to actuators and sensors one finds in cars and airplanes; all depend on ferroelectric materials. The unique property of ferroelectrics is that a block made of such material can form an electric potential across one of its dimensions (see Fig. 1). Applying an electric field to it can cause changes to this dimension even at very high frequencies. This allows the construction of ultrasound probes for example used in health care.

The control of the ferroelectric polarization ($\mathbf{P}$) with an external magnetic field ($\mathbf{H}$) in a material opens an enormous opportunity for new types of magneto-electric devices. The realization of such devices is based on multiferroic materials in which magnetism and ferroelectricity are combined and are strongly coupled. The number of multiferroic materials available is limited; however, recent advances have suggested that materials where magnetism is frustrated may offer an enhanced control of ferroelectricity with magnetic field. One of these new multiferroics – $TbMnO_3$ – exhibits a novel flop of its electric polarization from one direction to another when a magnetic field is applied. In these multiferroics, ferroelectricity arises as a secondary effect from the coupling of the lattice to a complex magnetic structure.

At the HMI, we used single crystals of $TbMnO_3$ and materials like it that we grow in our labs and apply high magnetic fields along all the dimensions that define their unique atomic arrangement. We found that the essential physics that describes this flop in the polarization arises from changes in the magnetic structure of the material.

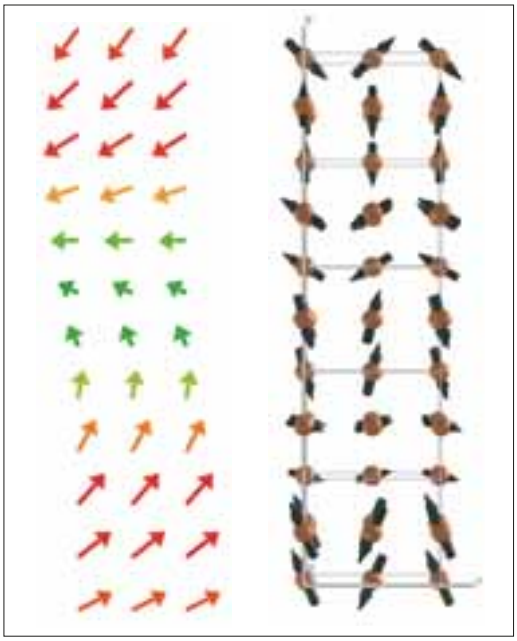

Fig. 2: Two examples of magnetic spin spirals. On the left, we illustrate the spin directions of a hypothetical spin spiral arrangement in a single layer of a magnet. Here, the direction of the magnetic moments spiral from pointing to the right at the bottom of the page to the left at the top. Similarly we show an illustration of the magnetic arrangement of $TbMnO_3$. Here the magnetic moments are tied to the manganese (Mn) atoms. In terms of symmetry, magnetic spin spirals can break inversion symmetry, a property that allows displacement of positively charge ions against negatively charged anions that make ferroelectricity possible in a crystal lattice.

Unravelling a spin spiral

The multiferroic properties of these materials arise from a complex arrangement of the magnetic moments of the manganese (Mn) ions. In simple terms, this complex arrangement can be described as a spiral as shown in Fig. 2. Theory tells us that magnetic materials such as these manganites become ferroelectric because magnetic moments in the manganese atoms organize themselves in such a spin spiral [1]. Theoretically, it works out that the symmetry of a spiral can break what is known as inversion symmetry and make ferroelectricity possible. To change the direction of the polarization with a magnetic field – and make a working device – theory tells us that we need to kick the spiral on its side. At the HMI, we have been investigating to see what happens when we apply high magnetic fields on these spin spirals to see if they indeed flop to their side. These measurements allow us to not only understand this mechanism better but also test the theory to see if it is correct. Our work on $TbMnO_3$ and $DyMnO_3$ showed a much more complicated behaviour than was anticipated. Firstly, when we apply a magnetic field in two ways we find a series of transitions from one magnetic arrangement to another which has a different periodicity [2] (by this we mean the characteristic length in which the spin arrangement repeats itself). This means that the spin flops in one or multiple steps (see Fig. 3). Secondly, we find that the magnetic moments on the terbium (Tb) and dysprosium (Dy) atoms also play a critical role both in the formation of the ferroelectric phase but also in helping it to flop the spiral with magnetic field [3].

Are the theorists right? Well, this is not clear. Our measurements find that once the spin spiral flops the magnetic structure may be a lot simpler than first thought. Indeed so simple that we have produced a straight forward model that explains the direction of the polarization without the need to use a complicated theory. However, these materials are relatively young and complicated and hold many surprises still.

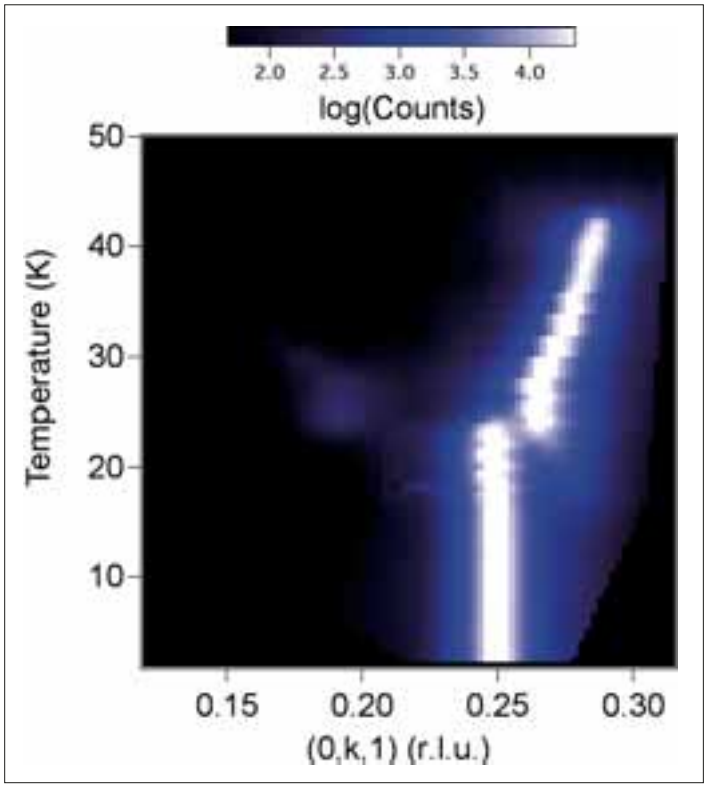

Fig. 3: Here, we show diffraction data measured from a single crystal of $TbMnO_3$ in a magnetic field of $10\,T$ applied parallel to the a-crystallographic axis. The colour image shows how a magnetic diffraction peak varies in position with temperature in the magnetic field. At high temperature, the periodicity is not a rational fraction and indicates that the length that this spiral needs to repeat itself is long $\sim 7\times$ the chemical unit cell. However, when the repeat changes discontinuously the spiral "shrinks" to a commensurate value of $4\times$ unit cell ($k = 1/4$).

[1] N. Aliouane, et al. Physical Review B 73, 020102 (2006)
[2] M. Mostovoy, Phys. Rev. Lett. 96, 067601 (2006)
[3] R. Feyerherm Physical Review B 73, 180401(R) (2006)

Corresponding author:
D. N. Argyriou
argyriou@hmi.de

Characterization of Precipitates in Inconel 706 Superalloys by Three-Dimensional Atom Probe and Transmission Electron Microscopy

N. Wanderka, V. Kindrachuk
■ 1 HMI, SF3

Fig. 1: Blades and discs of a gas turbine

Three-dimensional atom-probe (3DAP) is an analytical microscope able to map out the three-dimensional distribution of chemical species on an atomic scale [1, 2]. 3DAP makes it possible to measure quantitatively the chemical composition of small regions that can be selected arbitrarily in the reconstructed volume. In the present work, a three-dimensional atom probe was used to carry out a high resolution microchemical analysis of superalloys.

Due to its combination of high mechanical strength with good fabricability and machinability, the superalloy Inconel 706 (composition 40.68Ni-37.63Fe-17.52Cr-1.87Nb-1.85Ti-0.44Al (at.%)) is under consideration for ultra high temperature steam turbine applications (Fig. 1) with prospective steam temperatures up to 973 K. The alloy properties directly depend on the precipitation hardening process, which is based on precipitation of two kinds of A_3B-type compounds with different crystal structures. One kind of precipitate with the composition (Ni_3[Ti,Nb,Al]) is referred to as γ' phase, the other one with the composition (Ni_3[Nb,Ti]) as γ'' phase. Small γ' and γ'' precipitates about 15–20 nm in size as shown in Fig. 2 are embedded in a matrix consisting mostly of nickel and iron. However, these small γ' and γ'' precipitates in this alloy are metastable and transform into large laths of h phase (Ni_3[TiNb]) upon exposure to temperatures > 923 K. This process – usually called overageing – is accompanied by an unacceptable loss of creep and tensile strength.

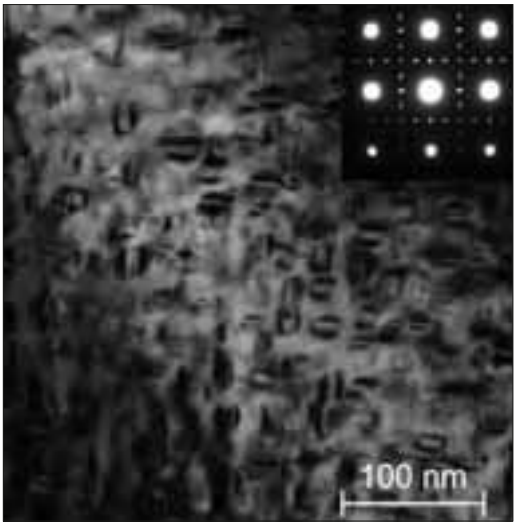

Fig. 2: Bright field TEM image of microstructure of Re-modified In-conel 706 alloy. Fine hardened γ', γ'' and γ'/γ'' precipitates embedded in the γ matrix can be observed. A [001] zone axis diffraction pattern is represented in the inset.

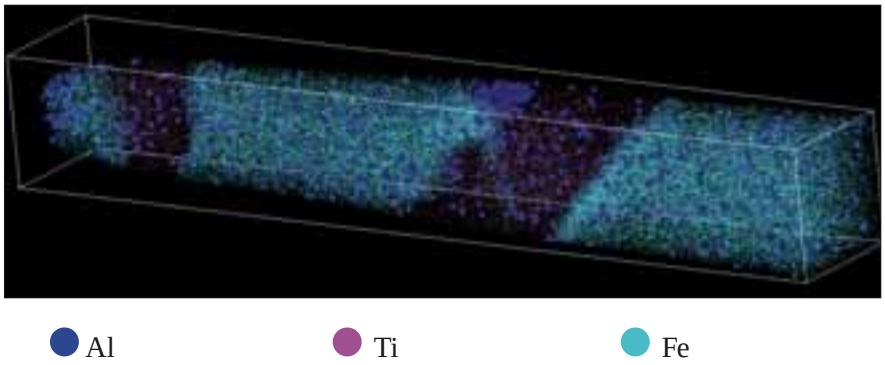

Fig. 3: Three-dimensional reconstruction of Re-modified Inconel 706 superalloy after ageing at 750°C for 750 h. The spatial arrangement of Al (dark blue), Ti (purple) and Fe (light blue) atoms in a volume of $14 \times 14 \times 235\,nm^3$ is shown, representing three γ′ precipitates embedded into the matrix.

In order to overcome this impasse, two different stabilization concepts were tested. On the one hand, it was attempted to create a diffusion barrier in the matrix surrounding the γ/γ′ precipitates by adding Rhenium to the composition of Inconel 706. Rhenium is known to effectively retard γ′ coarsening in cast single crystal Ni-base superalloys, as the interface segregation of the Rhenium strongly influences the stability of the precipitates. On the other hand, the [Ti+Al]/[Nb] ratio of Inconel 706 was specifically refined in order to minimize the thermodynamical tendency to transformation of γ/γ′ into the h phase. This modification was associated with a redesign of the Inconel 706 chemistry, resulting in a new alloy named DT706.

The microstructure of Inconel 706, Re-modified Inconel 706, and DT706 were investigated by means of electron microscopy (TEM) and 3 dimensional atom probe (3DAP) in the as-heat treated condition as well as after long-term exposure at 1023 K (Fig. 3). Results show that Rhenium was homogeneously dissolved in the matrix, but its partitioning ratio is too low to provide an effective obstacle to γ′/γ′ coarsening. In contrast, the microstructural degradation in DT706 (Fig. 4) was retarded as compared to Inconel 706, although the formation of h phase was not completely suppressed.

[1] A. Cerezo, T. Godfray and G. Smith, Rev. Sci. Instrum. **59**, 862 (1988)
[2] D. Blavette, A. Bostel, J. Sarrau, B. Deconihout and A. Menand, Nature **363**, 432 (1993)

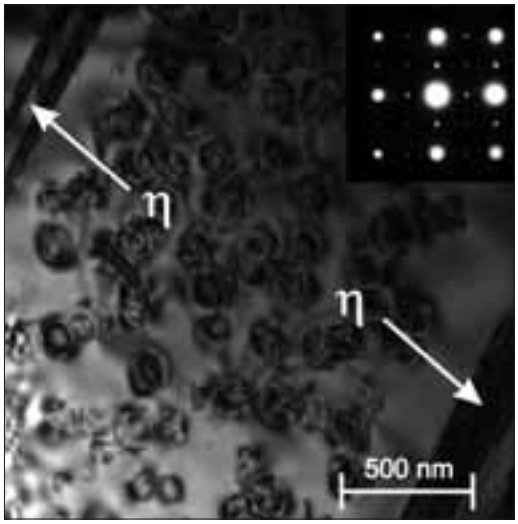

Fig. 4: Bright field TEM image microstructure of DT706 superalloy after ageing at 1023 K for 5000 h. Small γ′ cubes can be seen; additionally η phase is formed. A [001] zone axis diffraction pattern is given in the inset.

Fig. 5: A sample for the 3-dimensional atom probe (3DAP)

Corresponding author:
N. Wanderka
wanderka@hmi.de

Stroboscopic neutron scattering investigations of dynamics in nanosized magnetic systems

A.Wiedenmann[1], U.Keiderling[1], J. Haug[1], R.P. May[2], Ch. Dewhurst[2]
■ 1 HMI, SF3 ■ 2 ILL Grenoble

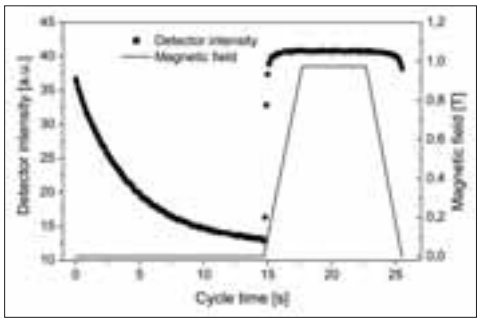

Fig. 1: Magnetic field and total detector intensity during the SANS experiment on Cobalt-Ferrofluid particles

Small angle neutron scattering (SANS) is an efficient method for investigating systems of nanosized particles that allows one to gain information about the size and form distribution as well as the ordering of the particles. Real-time investigations of time dependent processes in nanosized inhomogeneities by means of SANS, however, are usually limited to processes that are so slow that during data acquisition the system remains in a quasi-steady state.

For oscillating processes, stroboscopic SANS measurements are possible in short time slices when data collection can be synchronized with the periodic process. Here, we report on the set-up of a new time-resolved stroboscopic technique that allows relaxation processes to be studied at time constants of several $100\,\mathrm{ms}$, which are too fast for conventional SANS but by far too slow to be measured by quasi-elastic or spin-echo neutron scattering techniques. These methods are usually used for investigating time dependent processes with neutrons, but are appropriate for times below $<10^{-8}\,\mathrm{s}$ only.

An important field for studies of dynamic processes in nanosized particles are ferrofluids – magnetic liquids composed of magnetic particles a few nanometres large dispersed in a carrier liquid. The magnetic particles are coated by a surfactant stabilizing the liquid and preventing the particles from agglomerating. They can be investigated particularly well with polarized neutrons using a technique called SANSPOL developed at the Hahn-Meitner-Institut.

SANSPOL investigations of concentrated ferrofluids with cobalt cores (Co-Ferrofluids) have shown that an external magnetic field induces inter-particle interactions giving rise to pseudo-crystalline ordering of the magnetic particles [1]. Here, domains of local hexagonal arrangements coexist with fragments of spontaneously formed chains of particles with moments aligned along the external magnetic field. By using time resolved SANS in a stroboscopic mode we intended to follow the onset and decay of the local ordering when the field is switched on and off in order establish the kinetics of these processes [2, 3].

The investigations have been performed on SANS instruments at the Hahn-Meitner-Institut (V4) and at the Institut Laue-Langevin (ILL) in Grenoble, France (D22).

In the experiment, a concentrated Co-Ferrofluid sample was placed in a homogeneous horizontal magnetic field H applied perpendicular to the incoming neutrons. The scattering intensities $I(+)$ and $I(-)$ for polarized neutrons with incident neutron spin polarizations parallel and antiparallel, respectively, to the magnetic field were measured. At ILL, the magnetic field could be switched off from $0.5\,\mathrm{T}$ to the remanence of $0.005\,\mathrm{T}$ within less than $100\,\mathrm{ms}$. SANS measurements were performed in time-slices of $500\,\mathrm{ms}$ during a total time of $15\,\mathrm{s}$ after switching off the magnetic field. For raising and stabilisation of the field at $0.5\,\mathrm{T}$ a waiting time of $5\,\mathrm{s}$ was intercalated. Sufficient counting statistics were obtained after 400–600 cycles. At the HMI, a new readout system for the 2D detector is capable of producing data containing full position and time information for each single neutron. Extending a software package developed at HMI, these data allow for fully flexible control over the spatial and time resolution of the results *after* the experiments.

For the present case of superparamagnetic single domain particles the sum signal $(I(+)+I(-))/2$ contains contributions from magnetic disorder of individual particle moments and from inter-particle correlations. In the SANSPOL difference intensity $I(-)-I(+)$ all disorder scattering is cancelled leaving the nuclear-magnetic interference term which results solely from magnetic particles and which contains an anisotropic structure factor describing the inter-particle correlations.

In Fig. 1 the cycling of the magnetic field in the HMI experiment is plotted (solid line) together with the total detector intensity for the difference $I(-)-I(+)$. Each point has been calculated from one time frame with a width of 100 ms, after accumulation of approx. 700 cycles. The figure clearly shows the perfect statistics yielded by the presented stroboscopic technique. As soon as the field is applied, ordering sets in immediately and is nearly completed long before the field reaches the maximum. The ordering occurs so quickly that the limiting factor for the measured ordering kinetics appears to be the slope of the field up-ramp, rather than the native dynamics of the sample structure. Therefore, we do not discuss the ordering, but we emphasize that the presented technique easily allows the improvement of the time resolution *after* the experiment whenever, in a case like this, the first data processing results suggest that this may be useful. The scattering patterns measured at $H=0.5\,\mathrm{T}$ and $H=0$, respectively, turned out to be identical when measured in the stroboscopic cycling or in the static mode which demonstrated that the ordering-disordering process was really reversible. In Fig. 2 the 2D iso-intensity patterns of the sum $(I(+)+I(-))/2$ (left column) and the difference intensities $I(-)-I(+)$ (right column) are shown. After averaging the patterns of Fig. 2 at the angle $\alpha=30°$ with respect to the horizontal direction of the magnetic field over a width of $\Delta\alpha=20°$ the scattering intensities are plotted in Fig. 3 as a function of the momentum transfer Q. Fig. 2 and Fig. 3 reveal clearly the decay of the peaks indicating the local hexagonal order. In the final relaxation state, the intensities show a Q^{-1} dependence at low Q which is a characteristic feature of short fragments of dipolar chains. This shows that the hexagonal order gradually transforms into chain segments. Since the decay of the peak intensities was observed in the sum as well as in the difference patterns, we conclude that nuclear inter-particle correlations disappear simultaneously with the magnetic correlations. Further analysis shows that the structures decay exponentially with time with a characteristic relaxation time in the order of seconds. A detailed discussion of the basic relaxation mechanism in colloids is presented elsewhere [2, 3].

In summary the new stroboscopic SANSPOL technique allowed the nature of magnetic ordering of nanosized objects to be visualised during magnetic relaxation processes on a time scale of few hundred ms. In concentrated Co-Ferrofluids field induced magnetic and nuclear correlations were found to decay exponentially within a characteristic time of few seconds when the magnetic field is switched off. The local hexagonal particle arrangements with aligned magnetic moments transform gradually to uncorrelated segments of dipolar chains.

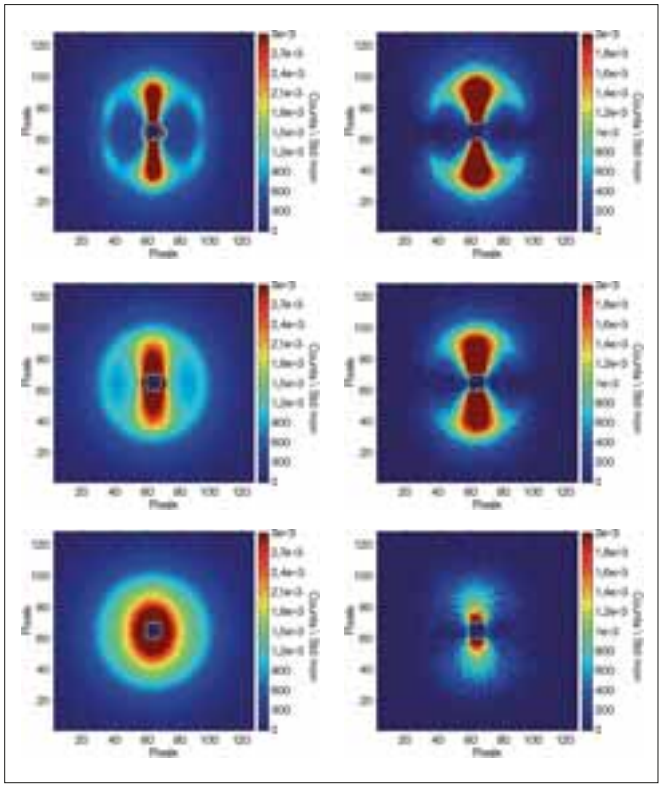

Fig. 2: 2D-SANSPOL Sum $(I(+)+I(-))/2$ (left) and Differences $I(+)-I(-)$ (right) at $t=0\,\mathrm{s}$, 2 s and 15 s after switching off the horizontal magnetic field of $0.5\,\mathrm{T}$. See text for details.

The project was supported by DFG Project Wi 1151/2 as part of the Priority program SPP 1104 (2000–2006).

[1] A. Wiedenmann, A. Hoell, M. Kammel, P. Boesecke Phys Rev. E 68, 031203, 1–10 (2003)
[2] A. Wiedenmann, U. Keiderling, R. P. May, C. Dewhurst, accepted in Physica B (2006)
[3] U. Keiderling, A. Wiedenmann, J. Haug, accepted in Physica B (2006)

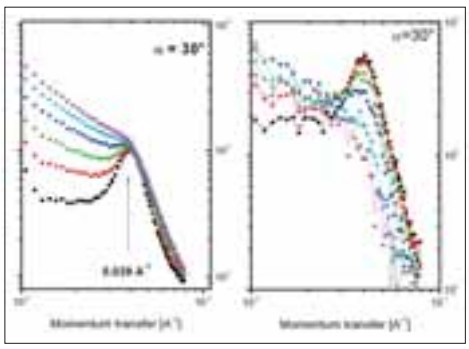

Fig. 3: SANSPOL intensity Sum $(I(+)+I(-))/2$ (left) and differences $I(+)-I(-)$ (right) in the sectors $\alpha=30°$ averaged over $\Delta\alpha=20°$ at $t=0.5\,\mathrm{s}$, 1 s, 1.5 s , 2.5 s , 5 s and 15 s after switching off the magnetic field of $H=0.5\,\mathrm{T}$

Corresponding author:
A. Wiedenmann
wiedenmann@hmi.de

Characterization of ion-beam induced nano-sized silver clusters in glass with synchrotron radiation

H.-E. Mahnke[1], B. Schattat[1], P. Schubert-Bischoff[2], N. Novakovic[1,3],I.Zizak[1]
■ 1 HMI, SF4 ■ 2 HMI, SF3 ■ 3 Research Institute VINCA, Belgrade, Serbia and Montenegro

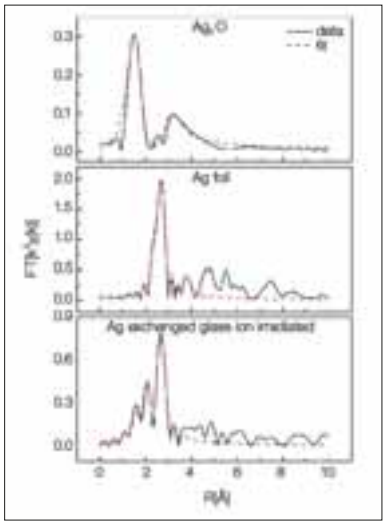

Fig. 1: Fourier transformed EXAFS signal (k2-weighted): The irradiated glass sample (bottom) shows the ion beam induced formation of metallic silver. The EXAFS signature for metallic silver (middle) and for Ag_2O (top) are given for comparison.

Glasses containing metal clusters have attracted attention both in cluster research and in possible applications of such clusters for magnetic or opto-electronic purposes. Nanometersized clusters of noble metals in glasses exhibit strong absorption of visible light which, in addition, may be highly polarization dependant depending on size and shape with special alignment of the clusters [1, 2]. Various preparation methods are pursued to obtain control of the mechanisms to form such clusters. A promising approach is the irradiation of glasses containing the wanted metal as a metal oxide with heavy-ion beams at energies of several MeV per atomic mass unit (i.e. per nucleon mass) [3, 4, 5]. At such velocities, the energy deposited along the ion path leads to the formation of tracks in the material. In the following, we show how synchrotron radiation techniques help to characterize materials modifications induced by ion beams.

We have studied the formation of clusters of metallic silver in soda lime glass induced by heavy ion irradiation with X-ray absorption spectroscopy (XAS), complemented with transmission electron microscopy (TEM) and with small angle X-ray scattering (SAXS). Silver was introduced by ion exchange into $0.1\,mm$ thick glass platelets (see [4]). While annealing under a reducing argon atmosphere with a few per cent of H_2 already leads to the formation of metal clusters, such clusters are not very uniform in size and are randomly distributed over the silver-containing glass volume. We have irradiated these silver-containing glass platelets kept at the temperature of liquid nitrogen with gold ions with energies of $600\,MeV$ with fluences around $10^{12}\,ions/cm^2$ at the Ion Beam Laboratory (ISL) of the Hahn-Meitner-Institut. The ion flux was kept below $10^{10}\,ions/cm^2s$.

Following the ion irradiation, the samples were investigated with X-ray absorption spectroscopy (EXAFS) at the Ag K-edge ($25.514\,keV$) either with or without further annealing at the same temperature as for the ion-exchange preparation under a reducing atmosphere (5% H_2-Ar mixture) for $30\,min$ (see Ref. [4]). EXAFS is a technique that allows deducing information on chemical bonds from details of the absorption spectra near the absorption edges. The EXAFS experiment was performed at the X1 beamline at the Hamburg Synchrotron Radioation Laboratory HASYLAB with the samples kept close to nitrogen temperature. The absorption was measured in fluorescence mode using a 7-element Ge detector. For comparison, the absorption was measured for samples of metallic silver and a sample of Ag_2O powder, mixed with graphite and polyethylene and pressed into a pill, too. The EXAFS spectra were analysed using the standard FEFF procedures [6, 7, 8] by which the coordination numbers and distances for at least the first and second coordination shells could be derived.

In Fig. 1, the ion-induced transformation from silver oxide into metallic silver is illustrated by the comparison of the different EXAFS signals. The extracted bond lengths correspond to the respective values known for the pure chemical systems. The bond length of Ag to O in the glass is slightly larger than in pure Ag_2O. This difference may reflect the substitution of Na by Ag as an impurity (details are presented in [9]).

As illustrated by the EXAFS spectrum, the transformation is not complete. Approximately 30% of the silver is surrounded by silver, while the major part of silver atoms is ambiented by oxygen. With no post-irradiation heat treatment the metal fraction is at the detection limit. Obviously, the metal

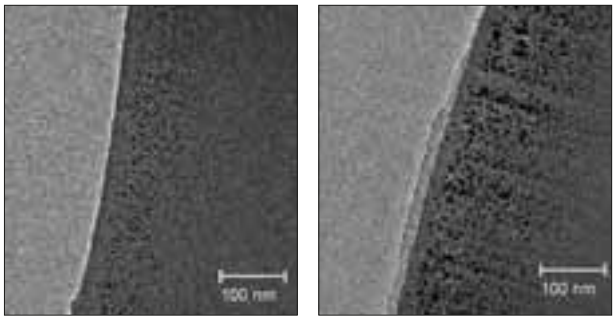

Fig. 2: Transmission electron microscope (TEM) picture of irradiated (right) and non-irradiated (left) glass samples: in the irradiated sample, after irradiation with gold ions and subsequent annealing. Clusters of metallic silver arranged in chains along the direction of the ion beamare visible. The TEM was operated at 120 kV.

fraction strongly depends on the treatment following the ion irradiation.

Complementary information on the distribution within the glass platelets, the shape and the sizes, was obtained from transmission electron microscopy (TEM) on thin slices of some 10 nm cut out of the samples parallel to the ion impact and deposed onto a fine grid. The comparison presented in Fig. 2 illustrates the significant influence of the ion irradiation: (i) the metal clusters have grown and their size distribution has become more uniform, but the most remarkable feature is that (ii) the clusters are arranged in chains parallel to the direction of the ion beam. Since some of the chains consist of clusters very similar in diameter and almost in contact, one is tempted to speculate that a totally columnar structure may be obtained by controlling the influencing parameters such as the ion fluence and the annealing parameters. A more quantitative description of the arrangement seen in the TEM pictures can be achieved by SAXS measurements performed at the newly commissioned 7 T multipole wiggler beamline of the Hahn-Meitner-Institut at the Berlin Synchrotron Radiation Source BESSY. An illustration of the first experiment is given in Fig. 3. The ion fluence in this case was 10^{11} cm^{-2}, the sample was heat treated after the ion irradiation in the same way as the sample in Fig. 2. A glass platelet without Ag also shows ion tracks when ion irradiated at nitrogen temperature. However, they disappear when the same annealing procedure is applied. Thus, the small angle scattering confirms the arrangement and shape of the Ag metal clusters as induced by the ion irradiation and proves to be a very valuable complementary way to study such ion induced structures.

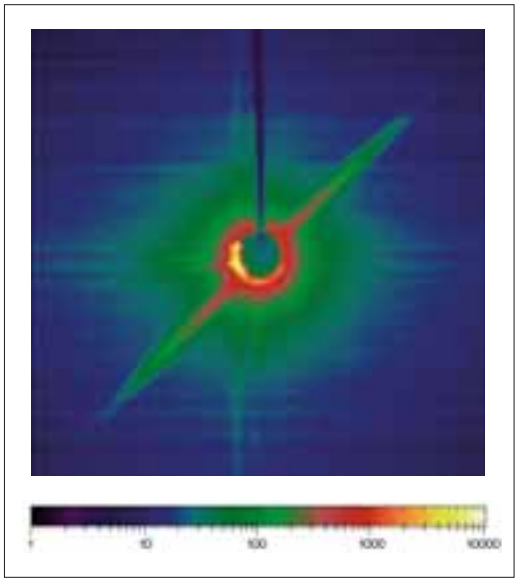

Fig. 3: SAXS image of the irradiated sample: In SAXS (Small Angle X-Ray Scattering) a cylindrical structure is represented by a disc, its length corresponds to the height of the disc and its diameter to the diameter of the disc. The dimensions in q space represented in the diagram correspond to a diameter of the “columns”, the arrangement of silver droplets along chains in the ion direction, of around 7 nm.

The authors are grateful to the HASYLAB staff at DESY, in particular to J. Wienold and E. Welter. We very much appreciate P. Szimkowiak’s help in sample preparation. Special thanks are expressed to the colleagues from SF3, especially A. Hoell, who were jointly in charge of setting up the SAXS beamline with one of the authors (I. Z.).

[1] K. L. Kelly et al. , J. Phys. Chem. B 107, 668 (2003)
[2] A. Podlipensky et al., J. Phys. Chem. B 108 , 17699 (2004)
[3] E. Valentin et al., Phys. Rev. Lett. 86, 99 (2001)
[4] G. Bataglin et al., Nucl. Instr. and Meth. in Phys. Res. B 200, 185 (2003)
[5] J. J. Penninkhof et al., Appl. Phys. Lett. 83 , 4137 (2003)
[6] J. J. Rehr et al., J. Am. Chem. Soc. 113, 5135 (1991)
[7] E. A. Stern et al., Physica B 208 & 209, 117 (1995)
[8] M. Newville et al., Phys. Rev. B 47, 14126 (1993)
[9] H.-E. Mahnke et al., Nucl. Instr. and Meth. in Phys. Res. B 245, 222 (2006)

Corresponding author:
H.-E. Mahnke
mahnke@hmi.de

Stochasticity in life: How microscopic fluctuations determine global behaviour of cells

M. Falcke, A. Skupin
HMI, SF5

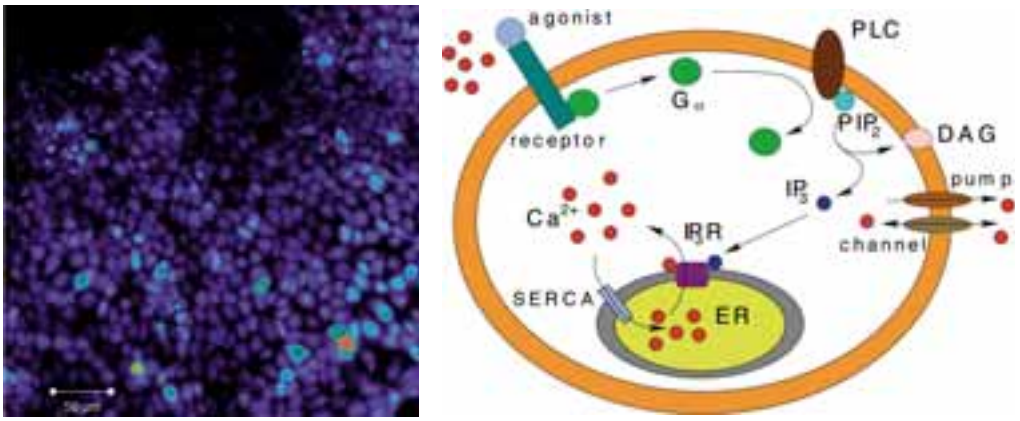

Fig. 1: Left panel: Microscopic fluorescence image of cultured astrocytes used in the investigation of calcium fluctuations in living cells. Red colour corresponds to high calcium concentration, blue to low concentrations. Right panel: Schematic illustration of a cell with the most important compartments for calcium oscillations: Calcium (red) can be released from the main calcium store, the endoplasmic reticulum (ER) (yellow), by ion channels. These channels are activated by calcium itself and IP_3 (blue), which is produced by a G-protein (green) induced phospholipase C (PLC). Due to this mechanism, cells are connected to their environment by the activation of the G-protein by external stimuli, like hormones or calcium.

There are different kinds of repeated events: Sunrise will come tomorrow for sure, and the next summer will happen for sure, too. We do not know when the next big thunderstorm will come, but we do know it is unavoidable. Similarly, the next snow avalanche will go down a mountain side with certainty – we only do not know which day. However, here we know at least that another one will not follow immediately at the same spot because snow has to build up first again on the mountain top.

Repeated events are common in signaling with chemical messengers inside and between living cells. They are perceived as a repeated increase of the messenger concentrations and are usually called oscillations. Calcium (Ca^{2+}) is probably the most ubiquitous second messenger, i.e. a messenger forwarding information arriving from outside within the cell [1]. It transmits its signal coded in the frequency of intracellular calcium concentration oscillations [2]. At the department Theoretical Physics (SF5), we investigate which type of repeated events these concentration peaks during oscillations belong to: Are they real oscillations like the up and down of the sun, really random events like a storm or random events with minimal temporal separation like avalanches? Theoretical research of recent years [3] had predicted the last one: Random events with a minimal time lag – a minimal interspike interval ISI.

The generation of a spike is a random event. After the minimal ISI has passed, it occurs with a certain probability per time unit. If this probability is large, it will occur very soon after the minimal ISI elapsed and the sequence of spikes will be rather regular with the minimal ISI as period. If the probability for spike generation is small, it will take longer till the next event and the spike sequence will be more irregular. In fact, if the average ISI is long, the standard deviation of the ISI is a linear function of the average ISI since spike generation is a Poisson process.

In intracellular Ca^{2+} dynamics, intracellular storage compartments take up or Ca^{2+} into the bulk of the cell (the cytosol) or take it up from there [4].

Release is controlled by channels on the membrane of the compartment. If a channel opens, Ca^{2+} leaves the storage compartment and the concentration in the cytosol increases. The channels have the peculiar property that their open probability increases with the Ca^{2+} on the outside of the storage compartment. Consequently, if one channel opens, Ca^{2+} diffuses towards neighbouring channels and they open, too. Thus, release is a self amplifying process. This self amplification causes the individual spikes of the oscillations. The cell is in a refractory state after such a spike during which the opening probability of the channels is very low. The next spike may occur after recovery from inhibition. That sets the minimal ISI.

The opening of the first channel is a random event. Due to increased Ca^{2+} density, the neighbours of this first open channel are more likely to open as well, but they will not open with certainty. Hence, the probability per unit time for opening of a sufficient number of channels for a global event may become rather small. However, if sufficiently many channels open, release spreads through the whole cell – a wave is initiated. On the molecular level, channel opening corresponds to a binding event of a Ca^{2+} ion or IP_3 molecule (Inositol triphosphate – another second messenger) at the cytosolic face of the channel. Hence, its randomness originates from the randomness of this binding event, i.e. thermal fluctuations. Typically, thermal fluctuations are averaged out, and on cellular level only deterministic behaviour is observed. The interesting property of intracellular Ca^{2+} dynamics is that fluctuations are carried through to the global level: The action of fluctuations can be read off the time series of global oscillations.

The most important prediction of recent theoretical investigations was that Ca^{2+} oscillations are repeated random events with a minimal ISI. That entails a linear dependence of the standard deviation of the ISI on the average ISI for large average ISI. We started a project in cooperation with several biochemistry laboratories: H. Kettenmann's laboratory at the Max-Delbrück-Centrum in Berlin-Buch, M. Wartenberg's laboratory at the GKSS outstation in Teltow outside Berlin, C. Taylor's laboratory at the University of Cambridge, and M. Bootman's laboratory at the Babraham Institute in Cambridge. The goal was to measure whether this theoretical prediction is verified by experimental data. Results from four different types of cells: astorcytes, micro glia, HEK cells (human embryonic kidney cells used in various experiments) and primitive endodermal cells confirm the theoretical prediction. Data from HEK cells are shown in Fig. 2. Clearly, the standard deviation σ increases with the average ISI.

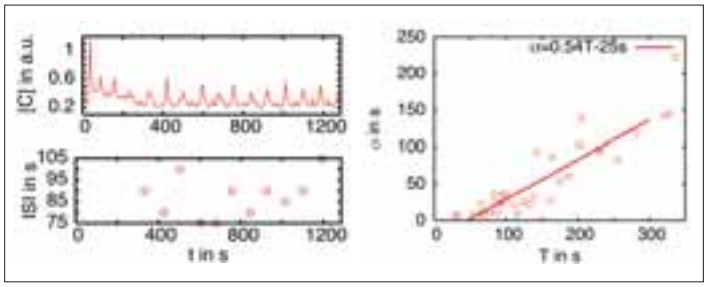

Fig. 2: A typical example of induced calcium oscillation in HEK cells (left top panel) and the corresponding inter spike intervals (ISI) (left bottom panel). By analyzing these oscillations, we derive a T-s-plot (right panel) showing the linear dependence of s on T verifying our assumption of a stochastic process within the cell.

The experimental data confirm that repetitive wave initiation is the mechanism creating sequences of Ca^{2+} spikes. That mechanism replaces the idea of the Ca^{2+} handling inside cells being a deterministic oscillator. These two mechanisms are fundamentally different and entail different dependencies of oscillation characteristics on cell properties. The route to a comprehensive theory of intracellular Ca^{2+} oscillations is clear now with these fundamental results and we will follow it up.

Intracellular Ca^{2+} dynamics has already been known as a prototypical pattern forming system. Now, the appeal of intracellular Ca^{2+} dynamics to physicists has acquired another aspect with the experimental confirmation of the wave initiation hypothesis. We can study the statistics of microscopic fluctuations with macroscopic measurements.

[1] Berridge, MJ., *Inositol trisphosphate and Calcium Signalling*, Nature 361, 315–325 (1993)
[2] Falcke, M., *Reading the patterns in living cells – the Physics of Ca^{2+} signaling*, Advances in Physics 53, 255–440 (2004)
[3] Falcke, M., *On the role of stochastic channel behavior in intracellular Ca^{2+} dynamics*, Biophys.J. 84, 42–56 (2003)
[4] Falcke, M., and D. Malchow, editors, *Understanding Calcium Dynamics – Experiments and Theory*, Lecture Notes in Physics, Vol. 623, Springer, Berlin Heidelberg New York (2003)

Corresponding author:
M. Falcke
falcke@hmi.de

The biological role of arsenic in the rat Combined studies using tracer technique and biochemical methods

K. Bukalis, D. Alber, G. Bukalis, D. Behne, A. Kyriakopoulos
■ HMI, SF6

The human population of many countries such as India, Bangladesh, Thailand, Taiwan or China is chronically exposed to arsenic through consumption of the water containing arsenicals [1]. This leads to a variety of health effects, which depend strongly on the dose of exposure, age, health-status parameters, and nutrition and vary greatly among individuals [2].

In particular, an extremely high cancer rate is observed in this population. Thus there is a strong evidence for carcinogenicity of arsenic in humans, but only weak evidence in the case of animals – a unique scenario different from the situation found for other carcinogens. At present there are no recognized models for the study of arsenic-induced carcinogenesis [3]. However, it has been convincingly established that arsenicosis (effect of chronic arsenic poisoning) is mediated through a modification of the gene expression, cell proliferation due to oxidative stress and other uncharacterized or poorly defined physiological aberrations or modifications [4]. The elucidation of such interactions might lead to the identification of sensitive subpopulations, provide cues for preventive or mitigation measures for arsenic intoxication, and suggest possible mechanism of toxicity.

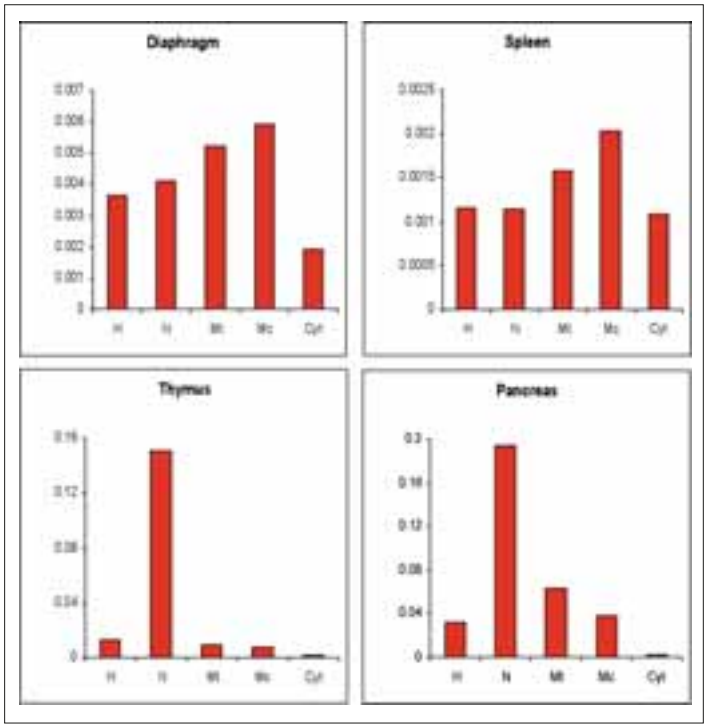

Fig. 1: Distribution of the ^{73}As in the homogenates and subcellular fractions of the diaphragm, spleen, thymus and pancreas; homogenate (H), nuclei (N), mitochondria (Mt), microsomes (Mc) and cytosol (Cyt)

Arsenic toxicity has been proposed to result from its affinity for the thiol groups of proteins. It has been reported that when arsenic is administrated to cells it initially binds to cellular proteins before reduction or methylation can occur [5]. Therefore, the binding of arsenic to cellular proteins is a key determinate in arsenic metabolism. Although numerous studies have attempted to isolate arsenic-binding proteins, non proteins from mammalian tissues have been identified and demonstrated to bind arsenic. It is of great interest to analyze the arsenic-containing proteins present in the tissues of the rat and to get information on their subcellular distribution and their biological effects.

As arsenic is present in the organism in very small amounts (total arsenic content in the human body $3-4\,\mathrm{mg}$), methods with extremely low limit of detection are needed in the investigation of the arsenic distribution among tissues and subcellular compartments and possible arsenic-containing proteins. For this purpose tracer methods, in which animals are labeled in vivo with ^{73}As, are very suitable (a tracer is a substance containing a radioactive isotope; often used for monitoring the biological processes). With a half life of 80.3 days and a gamma energy in the range of $53\,\mathrm{keV}$, this radionuclide is very well suited for tracer experiments. Because of the low detection limits of the tracer methods (below the femtogram range), only small amounts of the arsenic were used in experiments.

In order to obtain some information on arsenic sites of action and thus on its possible functions, the distribution of the tracer in the body compartments and their subcellular fractions was investigated. In this case rats were labeled *in vivo* by injection of 6 MBq ^{73}As (130 ng arsenic) per animal. After 48 hours the tissues were dissected and the activity of the tracer was determined using a scintillation detector. The ^{73}As-labelled tissues of the pancreas, thymus, spleen, liver, diaphragm, and lung were homogenized and than partitioned by differential centrifugation into nuclear, mitochondrial, microsomal and cytosolic fractions. The ^{73}As activity was related to the protein concentration of those compartments. The arsenic-containing proteins present in the homogenates of these tissues have been studied by gel electrophoretic separation of the proteins and autoradiographic detection of the tracer.

Our results show that the arsenic was distributed inhomogenously among the body compartments: the tissues varied strongly in the ^{73}As content. The element was preferentially taken up by the thymus, pancreas and diaphragm. The tissues with the highest arsenic retention were homogenized and than partitioned by differential centrifugation. In the homogenates and subcellular fraction of these tissues differences in the ^{73}As distribution were observed (see Fig. 1). The tracer was found to be incorporated differentially within the different cell compartments of the different tissues. It was mostly found in nuclei, but also in the cytosolic and microsomal fraction.

After combining tracer techniques with gel electrophoresis the arsenic-containing proteins could be detected in the homogenates of several rat tissues like spleen, adrenal gland, spermatic ducts, diaphragm, liver, thymus, trachea, brain, heart, lung, pancreas, testis, epididymis, small intestine and kidney. One of the autoradiograms is shown in Fig. 2. After evaluation of the autoradiograms several arsenic-binding proteins were distinguished. The protein labeled with ^{73}As had relative molecular masses of >250 kDa, 75 kDa, 50 kDa, 37 kDa, 29–30 kDa, 25 kDa, 16 kDa and 15 kDa (Da = amu). There were remarkable differences in the characteristics of the arsenic-containing proteins between the tissues after SDS-PAGE (sodium dodecyl sulphate polyacrylamide gel electrophoresis). The ^{73}As-binding bands with molecular masses of >250 kDa, 75 kDa, and 50 kDa were detected in all homogenates, whereas the bands of 37 kDa, 30–29 kDa, 25 kDa and 15 kDa were found only in some of them. The differences found in the distribution of the arsenic-binding proteins in the tissues indicate that the arsenic compounds may be involved in different intracellular processes. However nothing is known

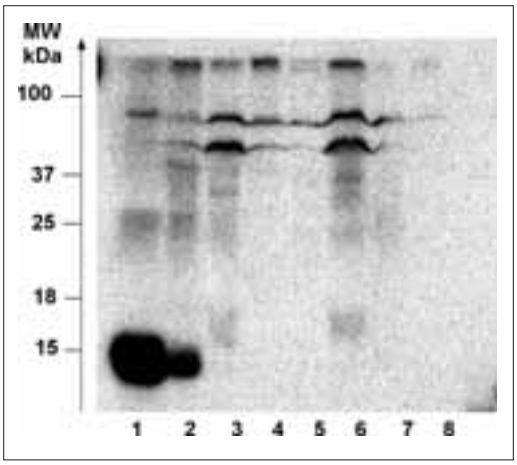

Fig. 2: Autoradiogram of the ^{73}As-labeled proteins in the blood (1) and homogenates of spleen (2), adrenal gland (3), spermatic ducts (4), diaphragm (5), liver (6), thymus (7), trachea (8)

so far about these proteins, their structure, and function and how arsenic is incorporated into them. All elements which are incorporated non-covalently into the proteins are lost during the electrophoresis because it is a denaturing separation method, which causes the proteins to lose their native structure. In case when ^{73}As remained in the proteins after SDS-PAGE the metalloid must be firmly bound, either covalently or as arsenosugar or one of the chemically active methylated compounds of trivalent arsenic.

The finding that arsenic is bound to proteins is of great interest. Therefore, further studies are being carried out in order to investigate more closely the biological functions of arsenic and especially the role of arsenic-containing proteins in different tissues.

[1] Jolliffe, D. M., Budd, A. J., Gwilt, D. J., *Massive acute arsenic poisoning*, Anaesthesia 46 (4), 288–290 (1991)
[2] Schoolmester, W. L., White, D. R., *Arsenic poisoning*, Southern Med J 73 (2), 198–208 (1980)
[3] Chen, C. J., Chen, C. W., Wu, M. M., Kuo, T. L., *Cancer potential in liver, lung, bladder and kidney due to ingested inorganic arsenic in drinking water*, Br J Cancer 66, 888–892 (1992)
[4] Barchowsky, A., Dudek, E. J., Treadwell, M. D., Wetterhahn, K. E., *Arsenic induces oxidant stress and NF-_B activation in cultured aortic endothelial cells*, Free Radic. Biol. Med. 21, 783–790 (1996)
[5] Styblo, M., Thomas, D. J., *Binding of arsenicals to proteins in an in vitro methylation system*, Toxicol Appl. Pharmacol. 147, 1–8 (1997)

Corresponding author:
K. Bukails
k.bukalis@hmi.de